



## D3.3: Seagrass and Macroalgae product



This project has received funding from the European Union's Horizon 2020 research and innovation programme under grant agreement No 776348.

**Project no.** 776348  
**Project acronym:** CoastObs  
**Project title:** Commercial service platform for user-relevant coastal water monitoring services based on Earth Observation  
**Instrument:** H2020-EO-2017  
**Start date of project:** 01.11.2017  
**Duration:** 36 months  
**Deliverable title:** D3.3: Seagrass and macroalgae product  
**Due date of deliverable:** Month 19  
**Organisation name of lead contractor for this deliverable:** UN (Partner 4)

**Author list:**

Name	Organisation
Maria Laura Zoffoli	UN
Pierre Gernez	UN
Laurent Barillé	UN
Vittorio Brando	CNR
Anne-Laure Barillé	Bio-Littoral
Nicolas Harin	Bio-Littoral
Steeff Peters	WI
Kathrin Poser	WI

Dissemination level		
PU	Public	X
CO	Confidential, restricted under conditions set out in Model Grant Agreement	
CI	Classified, information as referred to in Commission Decision 2001/844/EC	

History			
Version	Date	Reason	Revised by
01	24/05/2019	Sent to reviewer	GEO
02	31/05/2019	Sent back to UN	

# CoastObs Project

CoastObs is an EU H2020 funded project that aims at using satellite remote sensing to monitor coastal water environments and to develop a user-relevant platform that can offer validated products to users including monitoring of seagrass and macroalgae, phytoplankton size classes, primary production, and harmful algae as well as higher level products such as indicators and integration with predictive models.



*phytoplankton*



*seagrass*



*harmful algal blooms*



*primary production*

To fulfil this mission, we are in dialogue with users from various sectors including dredging companies, aquaculture businesses, national monitoring institutes, among others, in order to create tailored products at highly reduced costs per user that stick to their requirements.

With the synergistic use of Sentinel-3 and Sentinel-2, CoastObs aims at contributing to the sustainability of the Copernicus program and assisting in implementing and further fine-tuning of European Water Quality related directive.

# Partnership



Water Insight BV. (WI)



**UNIVERSITY OF  
STIRLING**

The University of Stirling (USTIR)



Consiglio Nazionale  
delle Ricerche

Consiglio Nazionale Delle Ricerche (CNR)



UNIVERSITÉ DE NANTES

Universite de Nantes (UN)



**UNIVERSITY  
OF APPLIED SCIENCES**

HZ University of Applied Sciences (HZ)



UNIVERSIDADE  
DE VIGO

Universidad de Vigo (UVIGO)



Bio-Littoral (BL)



**GEONARDO**  
STATE-OF-THE-ART AND BEYOND

Geonardo Environmental Technologies Ltd. (GEO)

## TABLE OF CONTENTS

1	Introduction.....	11
2	Study areas .....	12
2.1	Inter-tidal seagrass beds.....	12
2.2	Sub-tidal seagrass beds .....	13
3	Material and methods .....	17
3.1	Inter-tidal areas: data acquisition and processing .....	17
3.1.1	Field data for algorithm development .....	17
3.1.2	Image acquisition.....	19
3.1.3	Computation of seagrass seasonal cycle .....	19
3.1.4	Seagrass mapping .....	20
3.1.5	Epiphytes coverage.....	21
3.2	Sub-tidal areas: data acquisition and processing .....	23
3.2.1	Sensitive analysis to environmental factors.....	23
3.2.2	Field data for algorithm calibration.....	24
3.2.3	Image acquisition and processing .....	26
4	Preliminary results.....	28
4.1	Inter-tidal seagrass beds.....	28
4.1.1	<i>Z. noltei</i> seasonal cycle .....	28
4.1.2	S2 maps of seagrass percent cover and biomass .....	29
4.1.3	Epiphytes coverage.....	30
4.2	Sub-tidal seagrass beds .....	32
4.2.1	Environmental conditions .....	32
4.2.2	S2 maps of underwater seagrass, macroalgae and sand percent cover .....	34
5	Conclusions.....	37

6	Publications .....	38
7	References.....	39

## FIGURES

13	Figure 1 – (a) Location of Bourgneuf Bay along the French Atlantic coast. (b) S2 image acquired on the 16/07/2018 and displayed in RGB composition showing Bourgneuf Bay in its regional context. (c) Zoom on the three main seagrass meadows, identified as 1-3. (d, e) Field view of the seagrass meadow in Sep/2018.....	13
	Figure 2 – (a) Location of the Glénan Archipelago along the French Atlantic coast. (b) S2 image displayed in RGB composition. (c) Zoom on the Glénan Archipelago displayed in high spatial resolution and obtained from Google Earth. (d, e, f) Examples of different underwater substrate types found in the Glénan Archipelago: (d) <i>Sargassum</i> sp., (e) <i>Himanthalia</i> sp. and (f) <i>Zostera marina</i> . .....	14
	Figure 3 – (a) Location of the Venice Lagoon in Italy. (b) S2 image displayed in RGB composition and showing the Lagoon. (c, d, e) Seagrass beds observed in the field.....	15
	Figure 4 – Relationship between the S2-simulated <i>in situ</i> NDVI and the seagrass biological descriptors: seagrass percent cover and seagrass biomass .....	19
	Figure 5 – The diatom <i>Cocconeis scutellum</i> (a) is the main epiphyte of <i>Zostera noltei</i> leaves, (b) leaves can be covered by a monolayer of this diatom, (c) apex of the leaves colonized by a higher diversity of epiphytes.....	21
	Figure 6 – (a) Spectral signature of a <i>Zostera noltei</i> leaf colonized by the diatom <i>Cocconeis scutellum</i> . (b) transect along one leaf from the base not colonized by epiphytes to the highly colonized apex. .	22
	Figure 7 – Gradient of epiphytes colonization of <i>Zostera noltei</i> leaves along an intertidal transect from low to high (top) shore.....	23
	Figure 8 – Areas considered to evaluate environmental parameters in the Glénan Archipelago and in the Venice Lagoon.....	24
	Figure 9 – (a) Settings for substrate radiometry measurements during the field campaign in Glénan Archipelago in May/2018. Measurements were taken in samples of different pure substrates found in the archipelago: (b) sand, (c) brown macroalgae <i>Sargassum</i> sp. and (d) seagrass <i>Z. marina</i> . (e) Bottom albedo ( $A_b$ , dimensionless) measured <i>in situ</i> . .....	25

Figure 10 – (a) S2 NDVI seasonal cycle in Bourgneuf Bay intertidal seagrass bed, from March to December 2018. (b, c) *In situ* photos over inter-tidal *Z. noltei* beds during Summer and Winter, respectively..... 28

Figure 11 – The S2 image of the 14/09/2018 was used to map (a) the seagrass meadows in RGB color scale, (b) the NDVI, (c) the seagrass percent cover, and (d) the above-ground seagrass biomass. (d) Above-ground biomass (g DW m<sup>-2</sup>). (e) Zoom into a portion of the SPC map. .... 30

Figure 12 – (a) Position of the S2 samples selected to evaluate epiphytes coverage into the seagrass meadows. (b) R as a function of wavelength (nm) for the different samples considered in scheme a. (c) Slope estimated for the bands 740 to 783 nm for those samples. .... 31

Figure 13 – Annual variability of environmental parameters obtained from satellite data in the Glénan Archipelago and in Venice lagoon. (a) Chl concentration (in mg m<sup>-3</sup>); (b) Kd(490) (in m<sup>-1</sup>); (c) AOT (dimensionless) ; and (d) cloud fraction (dimensionless)..... 33

Figure 14 – S2-based Seagrass Density map in the Glénan archipelago ..... 35

Figure 15 – S2-based Sand Density map in the Glénan archipelago .....35

Figure 16 – S2-based Macroalgae Density map in the Glénan archipelago..... 36

## TABLES

Table 1 – Multispectral vegetation indices tested in this study to describe seagrass percent cover... 18

## Abbreviations

List of abbreviations	
Abbreviation	Explanation
AC	Atmospheric Correction
ACOLITE	Atmospheric correction for OLI 'lite'
ARVI	Atmospherically Resistant Vegetation Index
ASD	Analysed Spectral Device
C2RCC	Case2 Regional CoastColour
CDOM	Colored Dissolved Organic Matter
CMEMS	Copernicus Marine Environment Monitoring
DW	Dry Weight
EO	Earth Observation
ESA	European Space Agency
GIS	Geographical Information System
IQR	Interquartile Range
mND	modified Normalized Difference
MNF	Minimum Noise Fraction
NAP	Non-Algal Particles
NAS	Northern Adriatic Sea
NDAVI	Normalized Difference Aquatic Vegetation Index
NDVI	Normalized Difference Vegetation Index
NIR	Near Infrared
OBIA	Object-Based Image Analysis
R <sup>2</sup>	Coefficient of Determination
S2	Sentinel-2
S2A	Sentinel-2A
SAMBUCA	Semi-Analytical Model For Bathymetry, Un-Mixing, And Concentration Assessment

SAVI	Soil-Adjusted Vegetation Index
SDI	Substratum Detectability Index
SNAP	Sentinel Application Platform
SPC	Seagrass Percent Cover
SPC <sub>cores</sub>	seagrass percent cover estimated from in situ samples
SPM	Suspended Particulate Matter
SRF	Spectral Response Function
SWAM	Shallow Water Semi-Analytical Model
WAVI	Water Adjusted Vegetation Index
SB	Above-Ground Seagrass Biomass
mNDVI	modified Narrow-Band NDVI
IOPs	Inherent Optical Properties

## Symbols

List of symbols	
Symbol	Explanation
$A_b$	Bottom Albedo
AOT	Aerosol Optical Thickness at 500 nm
Chl	Chlorophyll-a Concentration
$E_d$	Downwelling Irradiance
error_f	Error Reached During Optimization
Kd(490)	Diffuse Attenuation Coefficient at 490 nm
Kd(550)	Diffuse Attenuation Coefficient for Downwelling Irradiance at 550 nm
$L_{core}$	Radiance Measured in situ in Core Samples
$L_{reference}$	Radiance Measured in a White Reference Spectralon
$L_{substrate}$	Radiance Measured Over Substrates
Rb(550)	Bottom Reflectance at 550 nm

$R_{insitu}$	Reflectance Of The Seagrass Cover Measured <i>in situ</i>
$R_{rs}$	Reflectance of Optically Shallow Waters
$R_{rs}^{\infty}$	Reflectance of Optically Deep Waters
$R_{sat}$	Bottom-Of-Atmosphere Reflectance Estimated From Satellite Information
$z$	Depth
$\delta\delta$	Second derivative
$\theta_w$	Solar Zenit Angle

# 1 Introduction

Seagrass meadows are ecosystems considered as blue-carbon sequesters and reservoirs that also play other important roles for the environment, acting as nursery and habitat for a variety of marine fauna, providing sediment stabilization through their rhizomes, favoring sedimentation of thin particles and regulating nutrient cycles and water turbidity. Seagrasses are considered as good indicators of environmental quality due to their sensitivity to environmental factors such as toxic substances, changes in nutrient concentrations, light availability and hydromorphology as well as their sessility (Neto et al., 2013). Thus, being seagrasses the only truly marine angiosperms, they are one of the indicators of the biological quality used to define the ecological status of transitional and coastal waters in the Water Framework Directive (Foden and Brazier, 2007). The metrics used to quantify the status of seagrass include the spatial extent and density of the beds and the number of species present, as well as the change of these parameters over time (Foden and Brazier, 2007). Despite their ecological importance and their recognized ecosystemic value, there are still high uncertainties in the quantification of areas occupied by seagrass ecosystems on the global scale and there is also a lack of understanding of their temporal dynamics.

Furthermore, another parameter that has been used in coastal ecosystems as an indicator of environmental quality, is the presence of epiphytes attached to macrophytes (Bricker et al 2003, Wood and Lavery 2000). Being epiphytes a microalgae, they present a fast response to nutrient load changes in the water column (Phillips et al. 1978, Frankovich and Fourquean 1997, Neckles et al., 1993, Murray et al. 2000, among many others). As a result, the higher the nutrient concentration in the water is, the higher the occurrence of epiphyte biomass. Thus, it is expected that in eutrophic areas or waters with reduced quality, epiphytes are found in higher abundances than in oligotrophic sites. Epiphyte coverage has also a direct negative effect on seagrass as they block the light availability needed in photosynthesis, reducing the gas diffusion through vegetal tissues and favoring the loss of leaves (Nelson, 2017).

The launch of the Sentinel-2 (S2) satellites has opened up new opportunities for consistent monitoring of coastal ecosystem quality by providing frequent high-resolution coverage. The objective of this task was to investigate the feasibility of accurately mapping both inter- and sub-tidal seagrass cover in coastal meadows using S2 satellite remote sensing. In inter-tidal seagrass meadows, the capabilities of S2 to detect epiphytes was also investigated .

## 2 Study areas

Three case studies were selected to perform seagrass/macroalgae mapping using high-resolution satellite remote sensing information. Bourgneuf Bay is located in an inter-tidal area, which means that it is exposed during the low-tide, while the Glénan Archipelago and the Venice Lagoon are located in the sub-tidal region, which means that they are constantly submerged.

### 2.1 Inter-tidal seagrass beds

Bourgneuf Bay (2°05'W, 47°00'N) is a macrotidal bay located along the Atlantic French coast south to the Loire Estuary, occupying a surface area of 340 km<sup>2</sup>, with about one third of its area corresponding to a large intertidal zone (Barillé et al., 2010) (Figure 1). The bay is characterized by a generally high turbidity, frequently having a concentration of suspended particulate matter (SPM) that exceeds 200g m<sup>-3</sup> in the northern sector. The southern part of the bay is moderately turbid, with SPM concentration typically ranging between 10 and 50 g m<sup>-3</sup> (Dutertre et al., 2009; Gernez et al., 2014). Due to the high turbidity, the benthic vegetation is generally not visible from above-water during high tide.

Monospecific seagrass beds of *Zostera noltei* are located in the south-western part of the bay, where the coastline is protected from the Atlantic swell by the Noirmoutier Island and by a rocky barrier (Figure 1c). Apart from seagrass, other classes of coverage can also be found there, but on a lesser extent: (i) bare sediment (sand and/or mud), and (ii) scattered patches of macroalgae brought by waves and not fixed to the substrate.

Bourgneuf Bay is a site of extensive aquaculture for the Pacific oyster *Crassostrea gigas* (Thunberg), with an annual production of about 5330 tons, ranking at the sixth place in France (Barillé et al., 2010). Several oyster farms are located nearby the seagrass meadows. The vicinity of oyster farms and the spatial interactions between aquaculture and the seagrass protected habitat is a concern for both the oyster industry and the environmental agencies. In the seagrass area, different species of bivalves (clams and cockles) are also extensively harvested for consumption and/or commercial purposes by local people, representing a hazard for seagrass populations due to habitat degradation by sediment digging (Bargain, 2012).

In Western Europe the seasonal cycle of *Z. noltei* is characterized by a unimodal distribution, with a maximum development in summer (Vermaat and Verhagen, 1996). The end of the summer season also corresponds to the highest spring tides period, with a maximum semi-diurnal tidal amplitude of about 6 m, thus maximizing the surface of emerged seagrass beds during low tide. Due to their accessibility for field measurements, we focused exclusively on the areas of seagrass meadows in the middle and southern portions of the bay (patches 2 and 3 in Figure 1c).

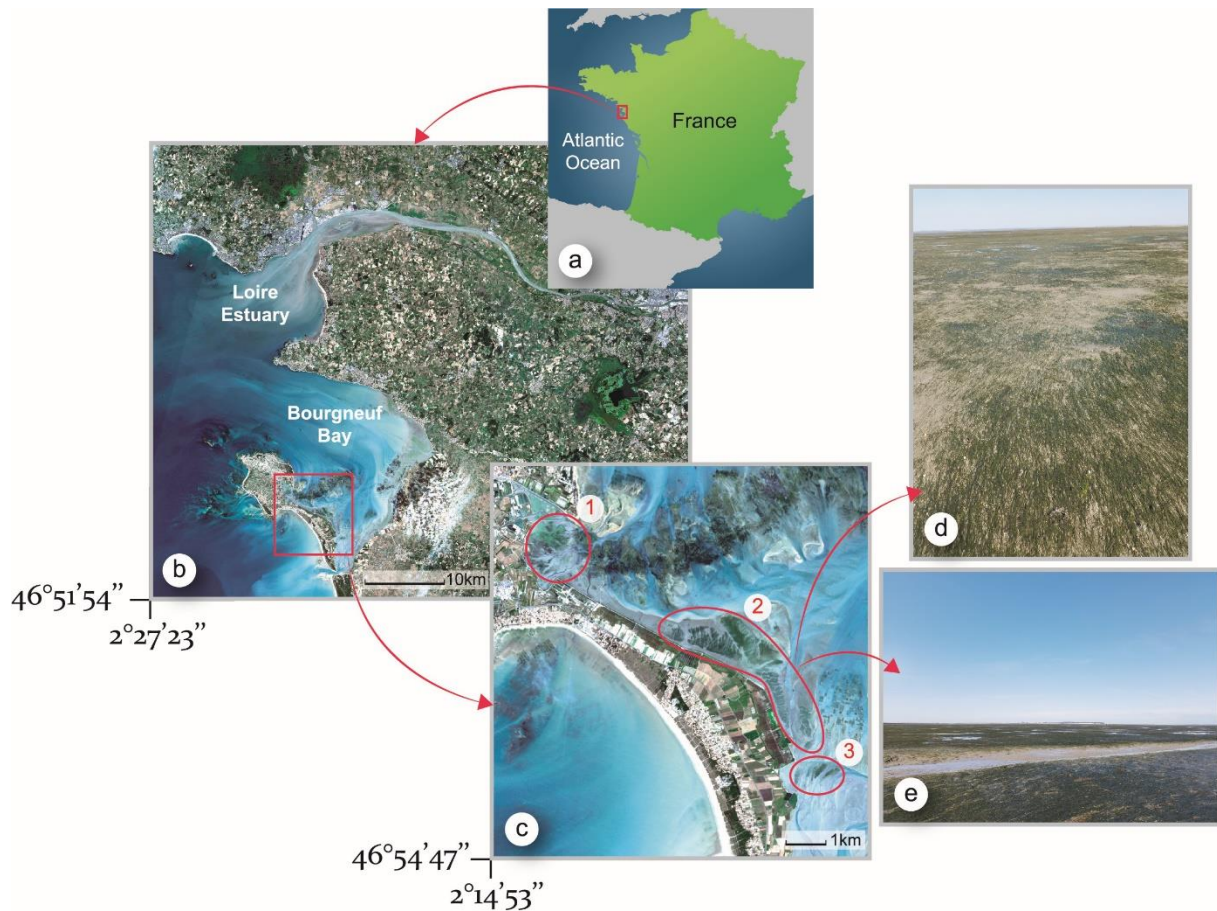


Figure 1 – (a) Location of Bourgneuf Bay along the French Atlantic coast. (b) S2 image acquired on the 16/07/2018 and displayed in RGB composition (R: 665 nm, G: 560 nm, B: 490 nm) showing Bourgneuf Bay in its regional context. (c) Zoom on the three main seagrass meadows, identified as 1-3. (d, e) Field view of the seagrass meadow in Sep/2018.

## 2.2 Sub-tidal seagrass beds

The two other sites, the Glénan Archipelago (Figure 2) and Venice Lagoon (Figure 3), present different complexities towards seagrass/macroalgae mapping. The permanent water layer covering these areas means that the signal received by the satellite includes information not only from the sea bottom but also from the water column above it. While waters in Glénan Archipelago are clear with much deeper light penetration and deeper distribution of benthic photosynthetic organisms, Venice Lagoon shows much more turbid waters and shallower substrates, constituting examples of different challenges to image processing.

The Glénan archipelago (47° 43' 01" N , 4° 00' 00" O) is located at nine miles from the coast in South Brittany, France. This area of ~35 km<sup>2</sup> is characterized by numerous rocky islets and nine small islands, surrounding an enclosed shallow lagoon protected from wave action. The site benefits from a temperate oceanic climate with less rainfall, a lower thermal amplitude and generally stronger winds than at mainland. In the archipelago, the tidal currents are low and the average tidal range is about 3m. The turbidity is low, generally between 2 and 4 NTU, allowing a good visibility from the surface to ~20 m depth. Nonetheless, the influence of the turbid plumes of the Loire and Vilaine can reduce water column transparency, especially during winter floods (Dutertre, 2012). Bottom substrates at Glénan Archipelago are constituted by macroalgae and seagrass beds of *Zostera marina*. *Z. Marina* is often found together with a sandy bottom in a stripped or "zebra" pattern.

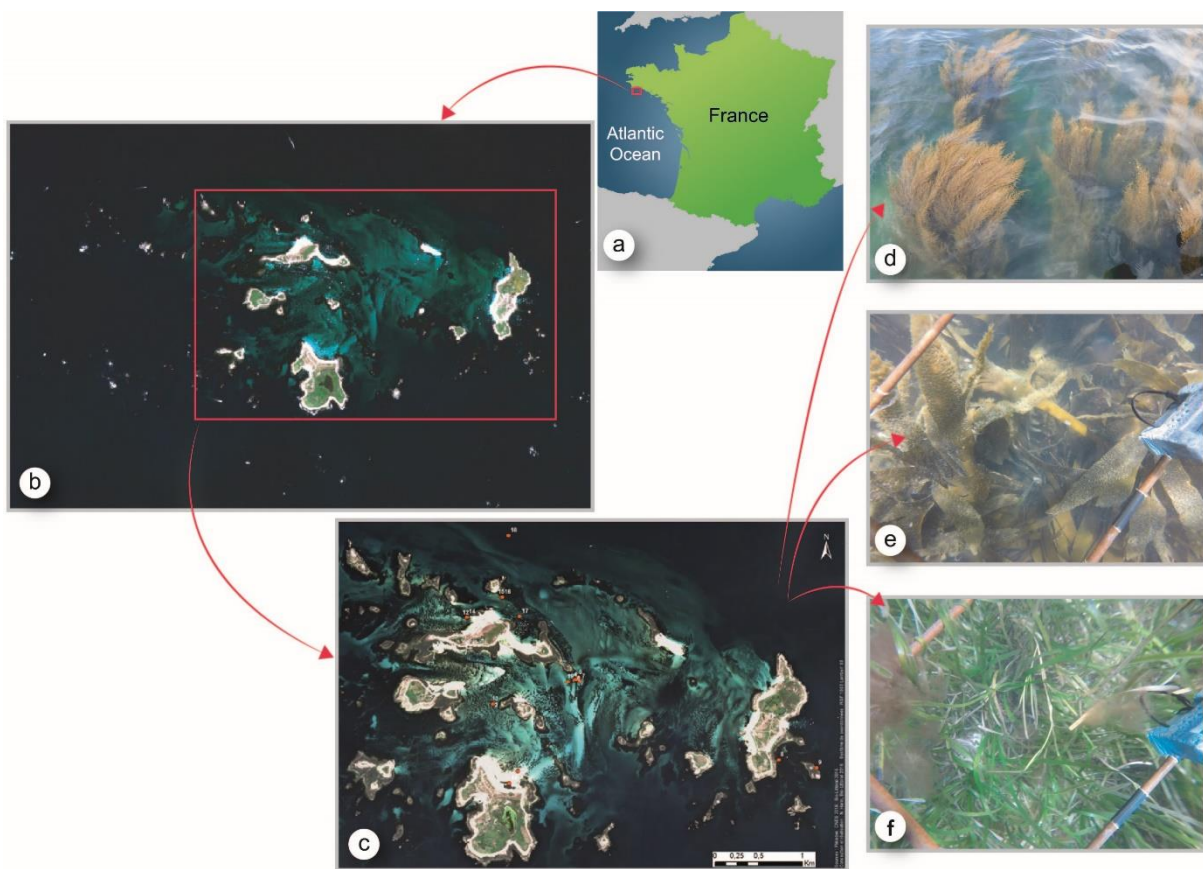


Figure 2 – (a) Location of the Glénan Archipelago along the French Atlantic coast. (b) S<sub>2</sub> image displayed in RGB composition (R: 665 nm, G: 560 nm, B: 490 nm). (c) Zoom on the Glénan Archipelago displayed in high spatial resolution and obtained from Google Earth. (d, e, f) Examples of different underwater substrate types found in the Glénan Archipelago: (d) *Sargassum* sp., (e) *Laminaria* sp. and (f) *Zostera marina*.

The Glénan archipelago is one of the three major seagrass meadow sites, with an area estimated in 14 ha, where there are also remarkable stands such as maërl beds made up of red algae like *Lithothamnion calcareum* and *L. coralloides*. The site is of exceptional interest in the sublittoral benthos, especially on bedrock (0 to 20 m) from very sheltered to very exposed areas, and with the presence of numerous rare animal species on a French scale (cnidarians, bryozoans, crinoids). The archipelago is protected by environmental regulations and its state of conservation is considered favorable.

The lagoon of Venice is a large and shallow coastal lagoon located in the Northern Adriatic Sea (NAS). It has a surface area of ca. 540 km<sup>2</sup> with an average water depth of about 1.1 m and a maximum tidal range of about 1.5 m. It maintains a connection to the NAS through the inlets of Lido, Malamocco, and Chioggia, and the exchange of water through the inlets in each tidal cycle is about a third of the total volume of the lagoon.

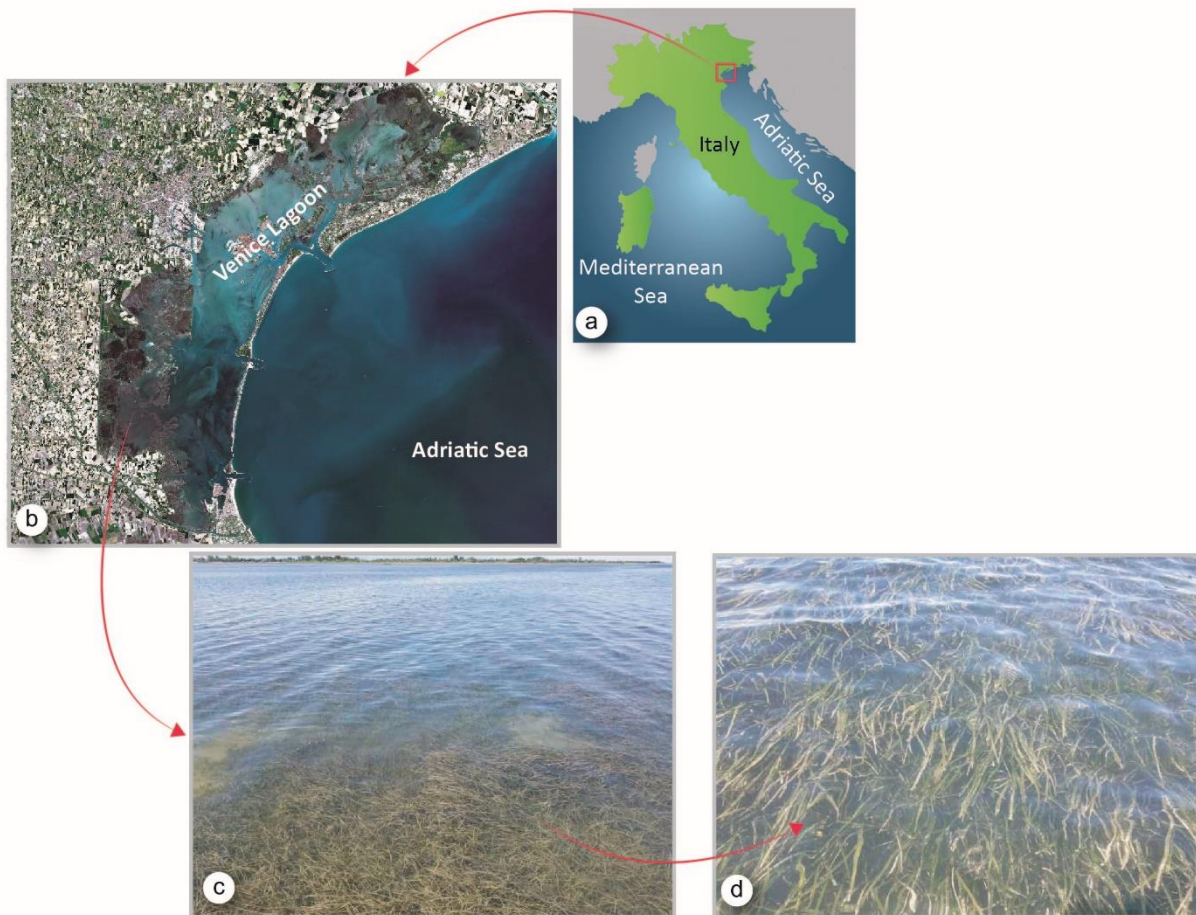


Figure 3 – (a) Location of the Venice Lagoon in Italy. (b) S2 image displayed in RGB composition (R: 665 nm, G: 560 nm, B: 490 nm) and showing the Lagoon. (c, d) Seagrass beds observed in the field.

The Venice Lagoon presents a heterogeneous morphology, characterized by a complex pattern of major (navigable) and minor channels, salt marshes, tidal flats and islands. Its bottom is covered by macroalgae beds and seagrass meadows of the species *Cymodocea nodosa*, *Z. marina* and/or *Z. noltei* (Scapin et al., 2018). The lagoon has been subjected to intense anthropogenic pressures during the 20th and 21st centuries, such as the construction of jetties at the inlets and dredging of the Malamocco– Marghera channel, which shifted the lagoon towards a prevalent erosion, leading to a negative sedimentary budget. Key ecological impacts include the extensive loss of benthic seagrass cover, areas subject to eutrophication, and anoxic crises.

## 3 Material and methods

### 3.1 Inter-tidal areas: data acquisition and processing

#### 3.1.1 Field data for algorithm development

Field sampling was performed at low tide on the 14 and 26/09/2018 in Bourgneuf Bay. A total of 35 sediment cores (20 cm diameter) was collected for algorithm development, spanning on a range of seagrass cover from bare sediment (0% of seagrass cover) to dense seagrass (100% of cover) during both days of our field trip. For each core, a nadir viewing above-ground picture of the seagrass surface was acquired prior to sampling using a field camera for subsequent determination of seagrass percent cover ( $SPC_{cores}$ ) through the 'ImageJ' software (Diaz-Pulido et al., 2011). Subsequently, the sediment below the core area was sampled up to a depth of about 20 cm, and each sample was sieved with a 1 mm mesh. Afterwards, the collected seagrass sample was sorted into leaves and rhizomes (above- and below-ground biomass, respectively), for measuring its dry weight (DW) after being dried for 48h at 60°C (Bargain et al., 2012; Barillé et al., 2010). For the rest of the study, only the above-ground seagrass biomass per unit surface (SB, in g DW m<sup>-2</sup>) was considered for consistency with remotely-sensed information.

On 14/09/2018, radiometric measurements at nadir were taken at the center of 20 cores prior to sediment sampling using an Analyzed Spectral Device (ASD Fieldspec) field portable spectroradiometer, measuring the radiance from 350 to 2500 nm ( $L_{core}$ ). Consecutively, radiance was also measured at nadir in the center of a white reference Spectralon ( $L_{reference}$ ). The reflectance of the seagrass cover ( $R_{insitu}$ ) was then estimated for each core station following Equation 1 (Milton et al., 2007).

$$R_{insitu} = \frac{L_{core}}{L_{reference}} \quad \text{Eq. 1}$$

Our dataset then consisted of a series of reflectance spectra varying over a range of seagrass percentage cover from 0 to 100%. The sky was consistently cloud-free during the field radiometric acquisitions and the measurements were performed avoiding shadows over the target. Reflectance spectra at hyperspectral resolution were then simulated to the multispectral resolution of Sentinel2A (S2A) using the sensor's spectral response function (SRF) (ESA, 2015), whereas the Normalized Difference Vegetation Index (NDVI; Tucker, 1979) was estimated from the red and near infrared (NIR) bands of S2A at respectively 665 and 842 nm (Equation 2). The decision to select the NDVI was made in consideration of several criteria. Firstly, the NDVI is a simple and well know index that could be applied to the majority of the historical and on-going Earth Observation (EO) satellite sensors, including those on-board the SPOT and Landsat missions. It therefore allows comparisons between our results and those from the literature. Secondly, the spatial resolution of a NDVI map computed using bands B4 and B8 is 10 m. Spectral indexes computed using other S2 spectral bands would be limited by lower spatial resolution (20 and 60 m), thus decreasing the accuracy of the seagrass maps or either restricted for some sensors that do not have a spectral band in the blue region (*e.g.*, SPOT).

Third, among various vegetation indexes tested, the NDVI produced one of the best fit (in terms of coefficient of determination,  $R^2$ ) with the seagrass percent cover (Table 1).

$$NDVI = \frac{R(NIR) - R(red)}{R(NIR) + R(red)} \quad \text{Eq. 2}$$

**Table 1 – Multispectral vegetation indices tested in this study to describe seagrass percent cover (SPC). For each spectral index, the equation and coefficient of determination ( $R^2$ ) between the in situ percent cover and the vegetation index are indicated ( $p < 0.01$  for all the linear regressions). The following indexes were compared: normalized difference vegetation index (NDVI), normalized difference aquatic vegetation index (NDAVI, Villa et al., 2014, 2013), water adjusted vegetation index (WAVI, Villa et al., 2014), soil-adjusted vegetation index (SAVI, Huete, 1988), atmospherically resistant vegetation index (ARVI, Kaufman and Tanré, 1992), modified narrow-band NDVI (mNDVI, Bargain et al, 2012) and modified normalized difference (mND, Sims and Gamon, 2002).**

Multispectral vegetation indices to describe SPC		
Index	Equation	$R^2$
NDVI(665,842)	$\frac{R(842) - R(665)}{R(842) + R(665)}$	0.989
NDVI(705,842)	$\frac{R(842) - R(705)}{R(842) + R(705)}$	0.987
NDAVI(490,842)	$\frac{R(842) - R(490)}{R(842) + R(490)}$	0.978
WAVI(490,842)	$(1 + 0.5) \frac{R(842) - R(490)}{R(842) + R(490) + 0.5}$	0.989
SAVI(665,842)	$(1 + 0.5) \frac{R(842) - R(665)}{R(842) + R(665) + 0.5}$	0.983
ARVI(490,665,842)	$\frac{R(842) - R(665) - (R(490) - R(665))}{R(842) + R(665) - (R(490) - R(665))}$	0.984
mNDVI(490,665,842)	$\frac{R(842) - R(665)}{R(842) + R(665) - 2R(490)}$	0.871
mNDVI(443,665,740)	$\frac{R(740) - R(665)}{R(740) + R(665) - 2R(443)}$	0.922
mND(443,705,740)	$\frac{R(740) - R(705)}{R(740) + R(705) - 2R(443)}$	0.931

A linear relationship was obtained from the field cores between the NDVI and the SPC (Equation 3, with  $R^2 = 0.99$ ,  $p < 0.001$ ) (Figure 4a). Furthermore, a non-linear relationship between seagrass biomass (SB) and NDVI was obtained (Figure 4b), and best modeled using a power function (Equation 4, with  $R^2 = 0.95$ ,  $p < 0.001$ ). In order to check the inter-annual variability of these relationships, a similar field sampling effort will be performed in September 2019. The final SPC and SB algorithms provided in the frame of CoastObs will be developed using the 2018 and 2019 *in situ* data.

$$\text{SPC} = 161.0027 \text{ NDVI} - 19.0058 \quad \text{Eq. 3}$$

$$\text{SB} = 279.65 \text{ NDVI}^{2.314} \quad \text{Eq. 4}$$

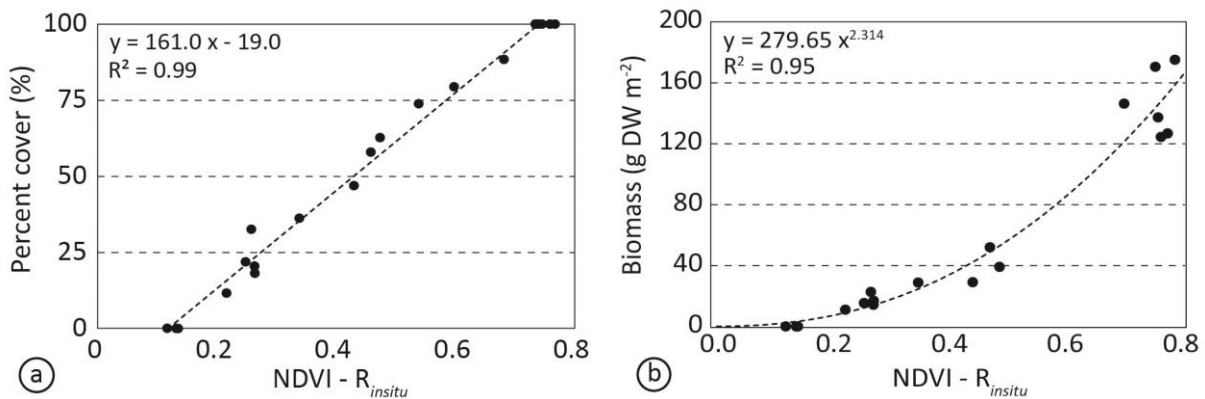


Figure 4 – Relationship between the S2-simulated *in situ* NDVI and the seagrass biological descriptors: (a) seagrass percent cover (SPC<sub>core</sub>) vs NDVI; (b) seagrass biomass (SB, g DW  $m^{-2}$ ) vs NDVI.

### 3.1.2 Image acquisition

Geolocated S2A/B images were freely downloaded from the European Space Agency (ESA) data portal (<https://scihub.copernicus.eu>) in Level 2A processing in 12/2018. Level-2A data already passed through atmospheric correction routines using the Sen2Cor processor algorithm (Main-Knorn et al., 2017) and were distributed as bottom-of-atmosphere reflectance ( $R_{sat}$ , adimensional). The whole S2 dataset used in this work comprises 22 images, acquired during free of clouds/shadows and low tide conditions (water level at the reference harbor < 3.20 m) between 30/03 – 10/12/2018. Two of these images coincided with field campaigns, on the 14 and 26/09/2018.

### 3.1.3 Computation of seagrass seasonal cycle

The NDVI was computed for all S2 images (Equation 2). A geographical mask was applied to exclude the land and ocean, and to select only the intertidal zone. Areas covered by macroalgae on rocky

substrate in the neighborhood of the seagrass beds were excluded based on Geographical Information System (GIS) data (Barillé et al., 2010). In order to select which date would be most representative of the annual growth peak, the seasonal variability of the NDVI was assessed using 22 low tide and clear sky S2 images.

For each S2 image, 15 clusters of 3 x 3 pixels (900 m<sup>2</sup>) were located within the seagrass meadow following some criteria and using as reference the image on 1/09, which was the image with the highest tide level among the summer images: (i) high NDVI ( $> 0.71$ ) in the reference image on the 1/09; (ii) located within an homogeneous area in terms of NDVI; and (iii) not biased by different height of tide. These criteria assured that we selected only high summer biomass / seagrass-dominated pixels, and that they were not covered by a layer of water during the satellite acquisition. The same stations were then extracted from the whole dataset. For each 3 x 3 pixel cluster, the median NDVI was computed, and the median and interquartile range (IQR) of the 15 extractions was calculated for each image. An averaged NDVI time-series was then built to assess the annual variability in 2018. A Gaussian model (two-terms) was fitted to identify the date of maximum NDVI peak, and the start of the decreasing phase. Additionally, we extracted pixels over an area of bare sediment to evaluate the background seasonal variability. Ten clusters of 3 x 3 “background” pixels were then selected using the image of the 1/09 as reference and considering the following criteria: (i) NDVI  $< 0.20$ ; (ii) located in homogeneous areas in terms of NDVI; and (iii) not biased by different height of tide.

### 3.1.4 Seagrass mapping

From the analysis of the S2-derived seasonal cycle of NDVI, the image of the 14/09/2018 corresponded to the annual growth peak. For this date SPC and SB were computed using the algorithms developed from *in situ* data (Equations 3 and 4). The maps were re-projected to Geographic Lat/Lon (WGS 84) Projection and all image processing was done using ESA’s Sentinel Application Platform (SNAP) (developed by Brockmann Consult, Array Systems Computing and C-S). From our model based in field sampling, it was observed that when the percentage of coverage was equal to zero, NDVI was about 0.12 due bare sediments and above-surface benthic microalgae associated with it which possesses some signals that raise the NDVI above zero (see Figure 4a). For this reason, SPC was set to 0 for NDVI  $< 0.12$ . Likewise, the percent cover was set to 100% for NDVI  $> 0.74$ . When the percent cover reaches 100%, the superposition of leaves is expected to increase the biomass, whereas the NDVI and the percent cover are expected to saturate. From the *in situ* dataset, NDVI seems to saturate at about 0.77, consistent with Barillé et al. (2010). As the *in situ* biomass dataset did not cover the full range of biomass to be found in the field, we relaxed the upper boundary of NDVI by +5%, and consequently extended the detection threshold up to 0.8. It is assumed that pixels with higher value do not correspond to seagrass, but to accumulation of drifted macroalgae (Barillé et al., 2010). In practice, no pixel with NDVI  $> 0.8$  was found within the seagrass area on the 14/09/2018, nor observed during the mean annual cycle.

### 3.1.5 Epiphytes coverage

*Z. noltei* leaves were collected in the inter-tidal seagrass meadow of Bourgneuf Bay. All samples were brought back to the laboratory in a cooler, preserved at 4°C in the dark and processed in less than 24h for spectral measurements with a hyperspectral imager. Microscopic examinations revealed that the leaves were mainly colonized by the diatom *Cocconeis scutellum* Ehrenberg (Figure 5), but that the apex of the leaves was colonized by a higher diversity of epiphytes.

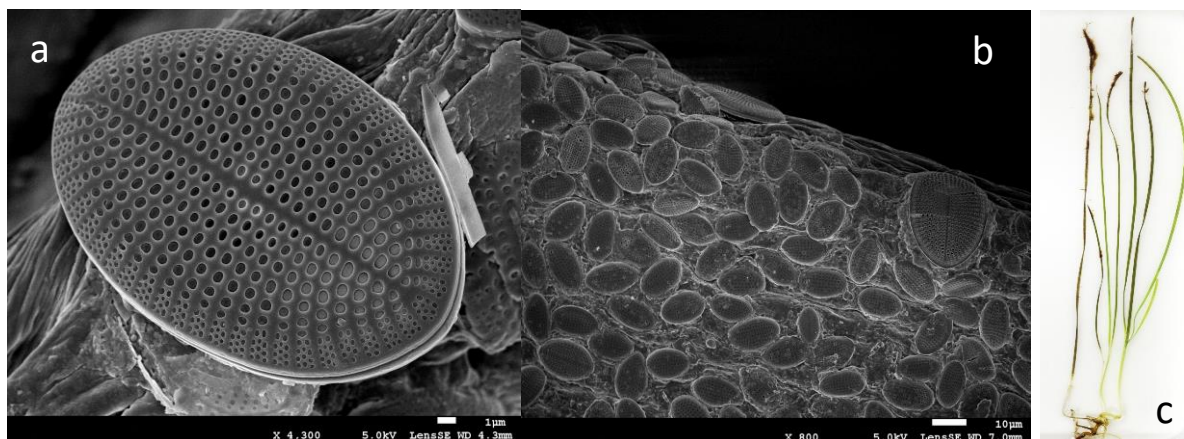
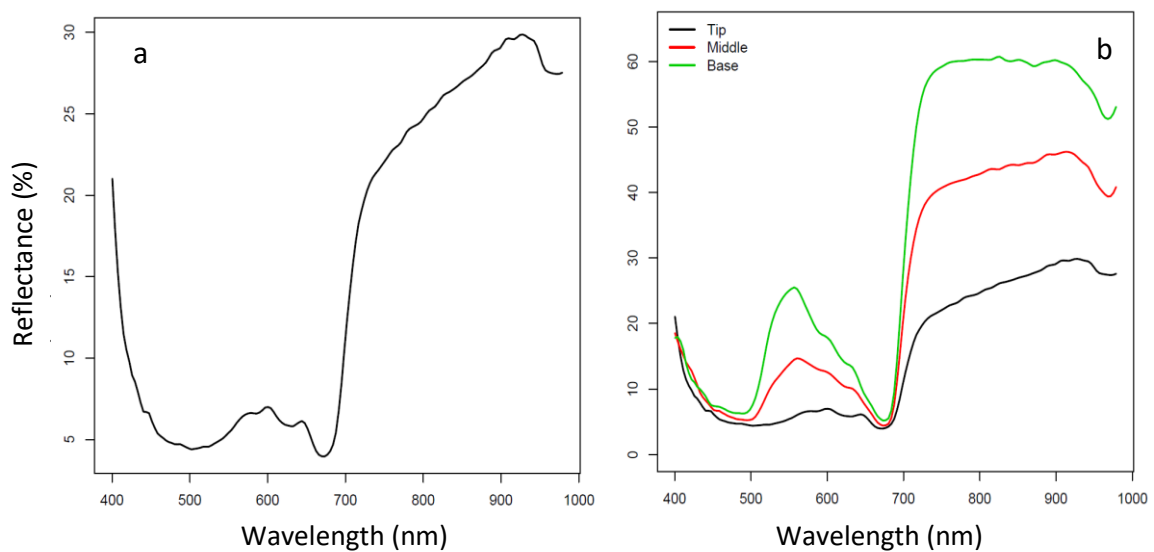


Figure 5 – The diatom *Cocconeis scutellum* (a) is the main epiphyte of *Zostera noltei* leaves (scale bar 1 µm), (b) leaves can be covered by a monolayer of this diatom (scale bar 10 µm), (c) apex of the leaves colonized by a higher diversity of epiphytes.

Hyperspectral images were acquired with a HySpex camera set up in the laboratory. The HySpex VNIR 160 camera has a spectral resolution of 4.5 nm and a spectral sampling of 3.7 nm in 160 contiguous channels between 400 and 950 nm. The camera was fixed at 1 m above the samples to obtain square pixels with a spatial resolution around 200 µm. Samples were isolated from the ambient light and the artificial illumination was controlled by two halogen quartz lamps (100 W). The optimal integration time was 20 ms to improve the signal-to-noise ratio. Reflectance was determined first by measuring the ratio between light reflected from a calibrated 20% grey reference panel (Spectralon®) and light reflected by seagrass leaves. Reflectance was practically calculated by dividing each pixel of the image by the mean intensity of Spectralon in the 400-950 nm wavelength range. Minimum Noise Fraction (MNF) transformations combined with a band pass filter of 9 nm were applied to images to remove noise and redundant information. Second derivative ( $\delta\delta$ ) images were calculated from the reflectance images following Jesus et al. (2014) and  $\delta\delta$  peaks were used to identify the main classes of photosynthetic epiphytes. These peaks corresponds to the main *in vivo* absorption features characteristic of a class. Namely,  $\delta\delta_{539}$  values were used to produce fucoxanthin images (diatoms proxy),  $\delta\delta_{568}$  to produce phycoerythrin images (red seaweed or rhodophytes proxy),  $\delta\delta_{648}$  to produce chlorophyll *b* images (host angiosperm proxy) and  $\delta\delta_{677}$  to produce chlorophyll *a* images (proxy of epiphytes plus host). It was possible to map the main class of epiphytes (diatoms, red algae) with the

spectral resolution of the Hypspec camera, but this is not possible with S2 resolution. However, it was noticed that when second derivatives identified a diatom biofilm, it was associated to a positive slope in the near infrared between 700-900 nm (Figure 6). This slope was not present when there were no epiphytes, which was the case with the base of each leaf (Fig 6b). We therefore hypothesized that this slope could be detected by S2 20 m NIR bands. Leaves imaged with the hyperspectral camera were also sampled at three sites along a transect from the high intertidal zone to the low intertidal zone. A significant gradient was observed with a higher colonization by epiphytes at the low intertidal site (higher immersion time) compared to the high intertidal site (lower immersion time) (Figure 7). This observation is consistent with the results obtained by Perkins *et al.* (2016).



**Figure 6 – (a) Spectral signature of a *Zostera noltei* leaf colonized by the diatom *Cocconeis scutellum*. Note the characteristic diatom absorption band of chlorophyll *c* at 632 nm and the steep NIR slope, (b) transect along one leaf from the base not colonized by epiphytes to the highly colonized apex (tip). Note the slope variation in the NIR. The characteristic angiosperm reflectance features between 500-600 nm is observed at the base of the leaf. This greenness tend to disappear with the presence of epiphytes.**

The same slope was explored into S2 images using the bands between 740 and 783 nm. Based on the seagrass coverage map on the 14/09/2018, pixels with SPC < 95% were masked out in order to warranty that the pixels considered in the analysis were covered exclusively by seagrass and not to include another targets (ex. bare sediment), which can equally alter the spectral response of the pixel. Also, these pixels presented high values of NDVI what indicates that none layer of water was affecting the pixel. From these pixels, some samples were selected in a gradient from upper to lower parts of the meadow following the gradient of abundance expected for epiphytes (Figure 7) and the  $R_{sat}$  at 740 and 783 nm (B6 and B7, respectively) was extracted. Finally, the slope between bands at

740 and 783 nm was calculated and contrasted to the position of the samples within the seagrass meadow.



Figure 7 – Gradient of epiphytes colonization of *Zostera noltei* leaves along an intertidal transect from low to high (top) shore. Leaves were imaged with a hyperspectral camera and the amount of epiphytic diatoms was estimated by the second derivative at 539 nm (a proxy of fucoxanthin pigment which is a biomarker of the class of diatoms).

Significant differences were observed for the 3 altitudinal level (ANOVA,  $P < 0.05$ ).  
(Courtesy of B. Jesus, University of Nantes)

## 3.2 Sub-tidal areas: data acquisition and processing

### 3.2.1 Sensitive analysis to environmental factors

We inspected long satellite time-series to analyze environmental conditions in sub-tidal areas and to evaluate when is the best time of the year to perform bottom mapping using satellite data. The parameters considered were: Chlorophyll-a concentration (Chl,  $\text{mg m}^{-3}$ ) as a proxy of phytoplankton biomass; Diffuse Attenuation Coefficient at 490 nm ( $K_d(490)$ ,  $\text{m}^{-1}$ ) as an indicator of water transparency; cloud fraction (dimensionless) and Aerosol Optical Thickness at 500 nm (AOT, dimensionless) indicating atmosphere interference. Cloud fraction and AOT time-series (2002-2018) were acquired from the Giovanni datasets (<https://giovanni.gsfc.nasa.gov/giovanni/>) and corresponded to a monthly average of some areas over both sites (Figure 8a, b) except for AOT in the Venice Lagoon, which was derived from an *in situ* sensor located at  $\sim 45^\circ\text{N}$ ,  $12^\circ\text{E}$  (AERONET network) and comprises a shorter period (2002-2007). In the case of Chl and  $K_d(490)$ , they were obtained from the Giovanni datasets in Glénan comprising the period 2002-2018 and from the Copernicus Marine Environment Monitoring (CMEMS) portal (<http://marine.copernicus.eu/>) in Venice (1997-2018). For Chl and  $K_d(490)$ , we worked under the assumption that the water column in deep areas in the

proximities of the seagrass areas present similar seasonal variability than shallow environments. Then, we estimated the monthly average in an area in the French Atlantic Coast and NAS (Figure 8c, d) to evaluate environmental characteristics in our study sites.

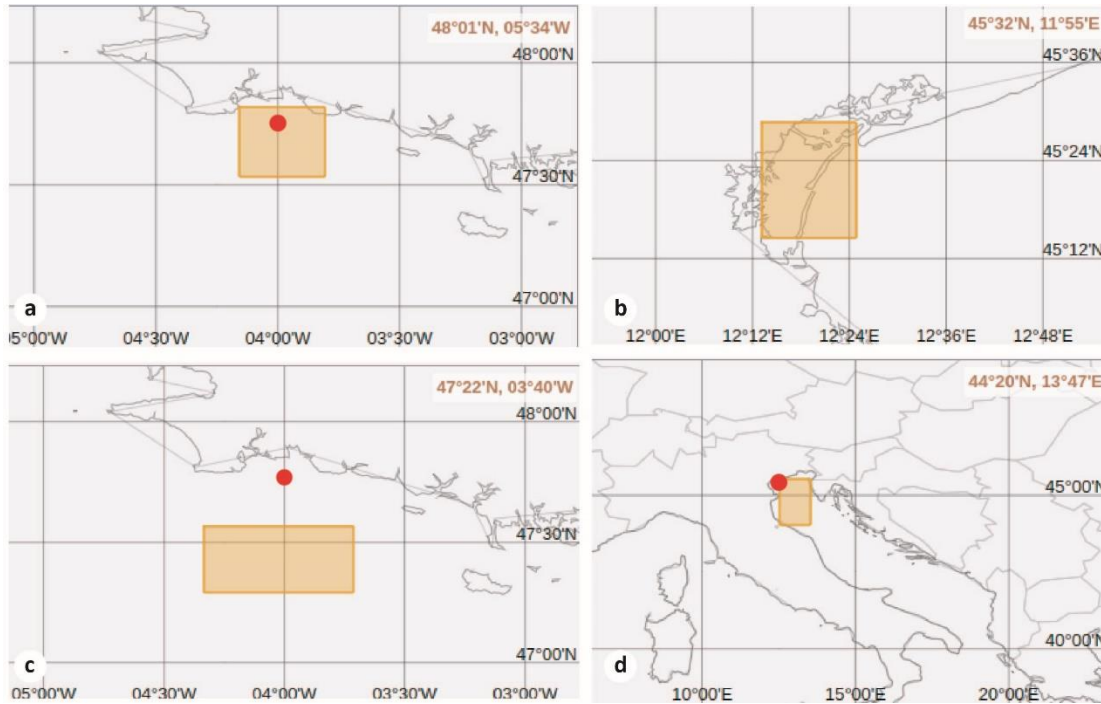


Figure 8 – Areas considered to evaluate environmental parameters. (a) for cloud fraction and AOT in the Glénan Archipelago; (b) for cloud fraction in the Venice Lagoon; (c) for Chl and  $K_d(490)$  in the Glénan Archipelago; and (d) for Chl and  $K_d(490)$  in the Venice Lagoon. In all the captures, red dots point the location of the study site.

### 3.2.2 Field data for algorithm calibration

Field sampling was performed at Glénan Archipelago from 29-30/05/2018. In this campaign, 7 calibration stations were considered: (i) for water column characterization in terms of Inherent Optical Properties (IOPs: absorption and backscattering coefficients) and biological information (pigment concentration and SPM); and (ii) to provide bottom albedo ( $A_b$ ) of representative bottom types to serve as end-members during water column correction processing (Figure 9). Radiometric measurements were taken using a WISP-3 instrument over pure substrates. Samples of such representative substrates namely bare sand, brown macroalgae (*Sargassum* sp.) and seagrass (*Z. marina*) were collected from the sea bottom and brought to the surface by scuba-divers. The radiometric measurements of these end-members were performed on the roof of the boat to avoid shadows and contamination in the  $E_d$  sensor coming from other structures in the boat.  $A_b$  was obtained as Equation 5.

$$A_b = \frac{L_{\text{substrate}} \cdot \pi}{E_d} \quad \text{Eq. 5}$$

where  $L_{\text{substrate}}$  (in  $\text{mW m}^{-2} \text{nm}^{-1} \text{sr}^{-1}$ ) corresponds to the radiance measured over different substrates and  $E_d$  (in  $\text{mW m}^{-2} \text{nm}^{-1}$ ) is the downwelling irradiance measured at the same time than  $L_{\text{substrate}}$ .

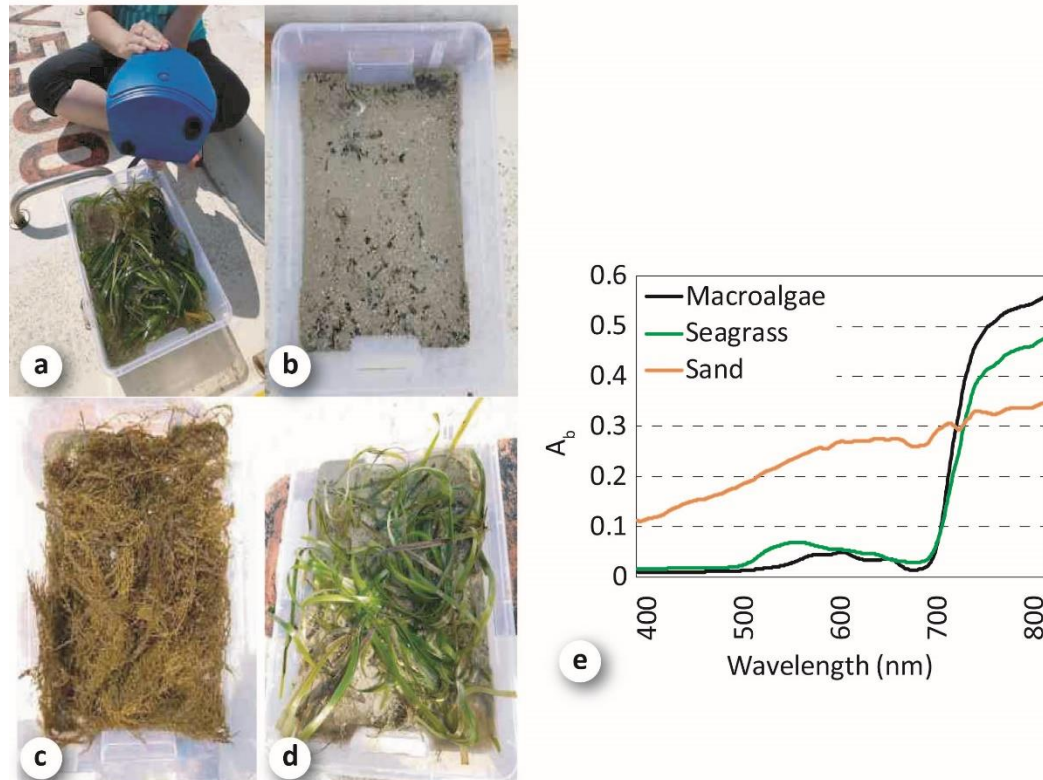


Figure 9 – (a) Settings for substrate radiometry measurements during the field campaign in Glénan Archipelago in May/2018. Measurements were taken in samples of different pure substrates found in the archipelago: (b) sand, (c) brown macroalgae *Sargassum* sp. and (d) seagrass *Z. marina*. (e) Bottom albedo ( $A_b$ , dimensionless) measured *in situ*.

In the Venice Lagoon, *in situ* water column characterization was performed between 8-9/05/2018 and 25-28/06/2018, both inside the lagoon and in coastal waters of the NAS in the proximities of the Venice Lagoon. During these campaigns, a total of 45 stations were considered. Parameters measured here included: remote sensing reflectance above-water ( $R_{rs}(0^+)$ ), IOPs (absorption and backscattering coefficients) and biological information (pigment concentration and SPM).

### 3.2.3 Image acquisition and processing

#### 3.2.3.1 Atmospheric correction

For both sub-tidal areas, cloud-free images were downloaded in Level 1C from the ESA's data portal (<https://scihub.copernicus.eu>). To obtain  $R_{\text{sat}}$  four different atmospheric correction schemes were tested: Atmospheric correction for OLI 'lite' (ACOLITE), the Case2 Regional CoastColour processor (C2RCC), POLYMER and the NASA approach available in Seadas. The first three models already showed good performance to correct atmospheric effects from S2 images over coastal and shallow waters (Caballero et al., 2019; Casal et al., 2019; Warren et al., 2019). The NASA AC method also showed a good performance to retrieve  $R_{\text{sat}}$  for OLI/Landsat8 images (Wei et al., 2018), thus being suitable for the correction of S2 data.

#### 3.2.3.2 Water column correction and bottom composition

The main challenge in shallow water remote sensing of submersed substrates arises from the fact that the signal detected by a remote sensor contains information not only from the bottom, but also from the water column. To properly compute the bottom information, satellite images over optically shallow waters have to be corrected for the influence of the water column (Dekker et al., 2006; Zoffoli et al., 2014). For this purpose, we applied the Shallow Water Semi-Analytical Model (SWAM), a publicly available tool distributed as part of the Sen2Coral plug-in in ESA's SNAP software for remote sensing studies of coral reefs in shallow waters (Wettle and Brando, 2006). SWAM implements the inversion of a bio-optical model and make use of optimization techniques to assess bottom properties from S2 images, retrieving at the same time and in each pixel both water column (absorption and backscattering coefficients) and bottom parameters (bathymetry ( $z$ ) and bottom reflectance).

The core of SWAM is based on the semi-analytical model for bathymetry, un-mixing, and concentration assessment (SAMBUCA) (Brando et al., 2009). This model starts with the algorithm proposed by Lee et al. (1999) for shallow waters (Equation 6), with some modifications to retrieve concentrations of Chl, CDOM (colored dissolved organic matter) and non-algal particles (NAP).

$$R_{rs} = R_{rs}^{\infty} \cdot \left( 1 - e^{\left[ -\left( \frac{1}{\cos \theta_w} + D_u^C \right) k \cdot z \right]} \right) + \frac{1}{\pi} \cdot R_b \cdot e^{\left[ -\left( \frac{1}{\cos \theta_w} + D_u^B \right) k \cdot z \right]} \quad \text{Eq. 6}$$

In Eq. 6,  $R_{rs}$  refers to reflectance of optically shallow waters,  $R_{rs}^{\infty}$  is reflectance of optically deep waters,  $\theta_w$  is the solar zenith angle,  $z$  is depth.  $k$ ,  $D_u^C$  and  $D_u^B$  are parameters that depend exclusively on the absorption and backscattering coefficients and then, they are related to light attenuation in the water column.

SWAM also account for bottom composition of mixtures of three different substrates. As a part of its processing SWAM/Sen2Coral decomposes  $R_b$  into the percentage of three bottom types or end-members, assuming that  $R_b$  is a linear combination of them. It was parameterized based on data collected in tropical coral reefs and by default those substrates are coral, macroalgae and sand. The

default outputs of the model are then:  $z$ , substratum detectability index (SDI), error reached during optimization ( $error\_f$ ), diffuse attenuation coefficient for downwelling irradiance at 550 nm ( $K_d(550)$ ), bottom reflectance at 550 nm ( $R_b(550)$ ), and percentage of coverage of the three end-members coral, macroalgae and sand.

Here, we adapted SWAM parameterization to the benthic classes found in our study areas using *in situ*  $A_b$  collected in the Glénan Archipelago: seagrass, brown macroalgae and sand. The bands used as input for SWAM/Sen2Coral were exclusively those between 443 – 705 nm. Pixels with  $SDI < 5$  were masked out considering that bottom contribution to the remote sensing signal in those pixels was negligible. The percentages of the three substrates were reclassified into: absence (0-5%), low coverage (5-30%), medium coverage (30-60%) and high coverage (60-100%).

### *3.2.3.3 Bottom mapping using classification techniques*

The bottom decomposition performed by SWAM/Sen2Coral uses an unmixing spectral linear model that takes into account the spectral information only. It means that it strongly relies on the spectral discrimination of the classes at the spectral resolution of the sensor considered. It is different from classification techniques that allow to incorporate knowledge of the area and spatial patterns. The result of applying a classification algorithm is a map which includes a number of thematic classes that can be defined *a priori* by the user (when classification is supervised). Depending on the algorithm adopted, it can be pixel-based or based on clusters or segments that present similar characteristics. Here, SWAM/Sen2Coral will be run in a Python stand-alone version to set different outputs under demand of the user. Information of  $R_b$  in five of the S2 bands (443 – 705 nm) will be retrieved and in turn, used as inputs for different classification schemes. Supervised classification algorithms will be tested, including neural networks and Object-Based Image Analysis (OBIA).

## 4 Preliminary results

### 4.1 Inter-tidal seagrass beds

#### 4.1.1 *Z. noltei* seasonal cycle

In 2018, a total of 22 S2 low-tide images was used to characterize the seasonal variability of NDVI over the seagrass meadow. The dataset combined images from two different orbital cycles (#137 and #94) and two sensors (onboard S2A and S2B). We did not observe any significant difference between the orbits and/or sensors (Figure 10a), suggesting that the S2 time-series is robust enough to characterize the seasonal dynamics of intertidal seagrass meadows. The average NDVI exhibited a clear seasonal cycle, with a late-summer maximum and a winter minimum as expected for inter-tidal seagrass meadows in the West coast of the North Atlantic Ocean (Vermaat and Verhagen, 1996).

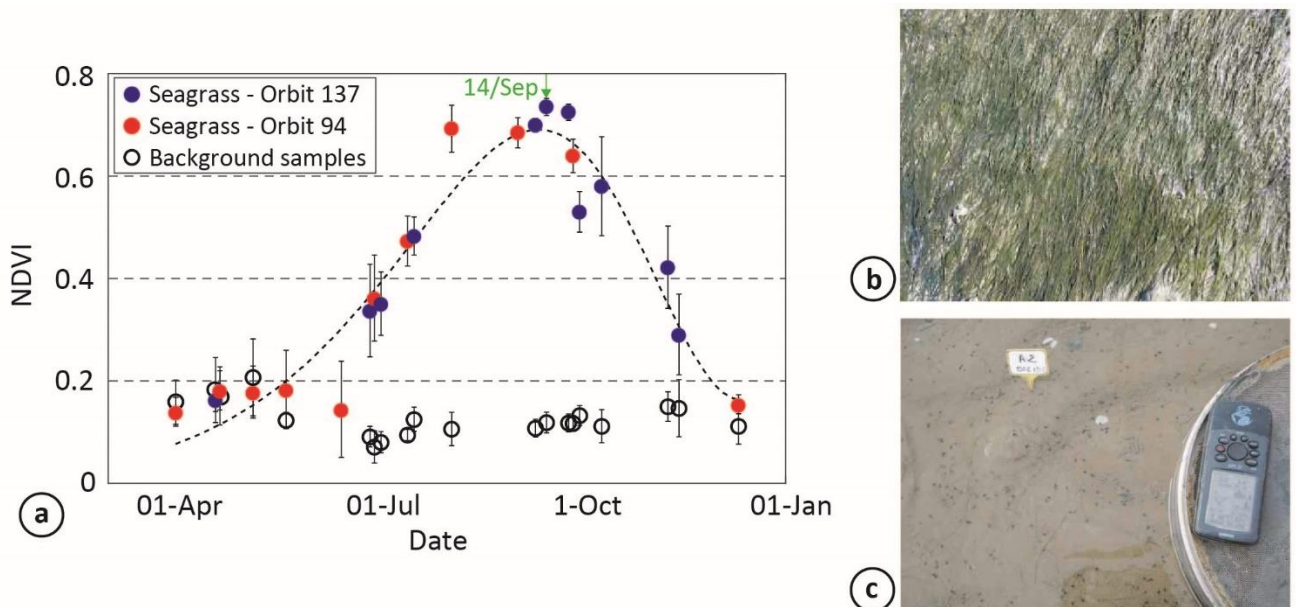


Figure 10 – (a) S2 NDVI seasonal cycle in Bourgneuf Bay intertidal seagrass bed, from March to December 2018. Red and blue symbols correspond to the NDVI of the seagrass pixels (median  $\pm$  IQR), with the dashed line corresponding to a two-term Gaussian model. Bourgneuf Bay is located at the overlap between two orbital cycles, with orbits #137 and #94 in blue and red, respectively. Black symbols correspond to the background pixels extracted over bare sediment (median  $\pm$  IQR). No distinction of orbit has been done for the background pixels. (b, c) *In situ* photos over inter-tidal *Z. noltei* beds during Summer and Winter, respectively.

There was some variation for the background pixels corresponding to an area of bare sediment outside the seagrass meadow (black symbols in Figure 10a). The background annual NDVI did not exceed a value of 0.24 and was highest during spring. Such a seasonal pattern is consistent with the expected annual cycle of benthic microalgae in Bourgneuf Bay (Echappé et al., 2018). During early spring and winter, the NDVI time-series of the seagrass meadow is similar to that of the background pixels, suggesting at least a substantial reduction, if not a complete loss, of the seagrass biomass (Figure 10b and c). The spring and winter values are indeed below the lowest NDVI boundary considered by Barillé et al. (2010) to detect sparse seagrass, and very likely correspond to benthic diatoms or bare sediments.

We then applied a Gaussian model (two-terms) to the NDVI time-series to better appraise the seagrass phenological cycle (dashed line in Fig. 10a, with  $R^2 = 0.92$ ,  $p < 0.001$ ). Following a criteria of 10% increasing in the fitted Gaussian function with respect to the baseline value, we defined the growing season starting on 12/05/2018 and ending on 3/12/2018 (Jönsson and Eklundh, 2004). Interestingly, the data dispersion in terms of IQR was higher during the increasing and decreasing phases than during the summer maximum, suggesting heterogeneous dynamics of growth and loss within the various seagrass patches of the meadow. The seagrass maximum occurred the 10/09, and NDVI remained within 5% of the maximum from 22/08 to 28/09.

#### 4.1.2 S2 maps of seagrass percent cover and biomass

Based on the analysis of the seasonal variability, the S2 image of the 14/09/2018 was selected to compute the SPC and SB maps because it was the date closest to the annual maximum. SPC and SB were estimated from this NDVI image based on parameterizations proposed in Equations 3 and 4, respectively. The maps of seagrass percent cover and biomass are shown in Figure 11.

The SPC map exhibited a nearly uniform amount of pixels in the gradient from 0 – 100% (Figure 11c), with a meadow-averaged SPC of 44.7%. The area corresponding to  $SPC > 50\%$  occupied a surface area of 1.95 km<sup>2</sup>, from which about 0.74 km<sup>2</sup> had a cover  $> 80\%$ . Areas of low percent cover were generally observed close to the waterfront, whereas the areas of highest seagrass density were located from the middle of the meadow towards the upper limit of the intertidal zone. Superimposed over the general altitudinal pattern, the spatial distribution of seagrass cover exhibited several patterns at a smaller scale. Areas with low SPC were observed along the intertidal channels that orthogonally streaked the seagrass meadow (Figure 11e, and see also picture in Figure 1e). Small areas of very dense seagrass cover were also found at several spots, whose patchy distribution could be attributed, at least partially, to the clonal growth of seagrass around dense spatial kernels.

The map of above-ground seagrass biomass exhibited values ranged from 2 – 166 g DW m<sup>-2</sup>, and the meadow-averaged biomass (42 g DW m<sup>-2</sup>) was shifted toward the lower range (Figure 11d). An altitudinal distribution was also observed, with the patches of highest biomass generally located nearshore. The influence of the intertidal channels is also clearly visible on the map of biomass, and many clusters of high biomass are separated by the network of intertidal canals.

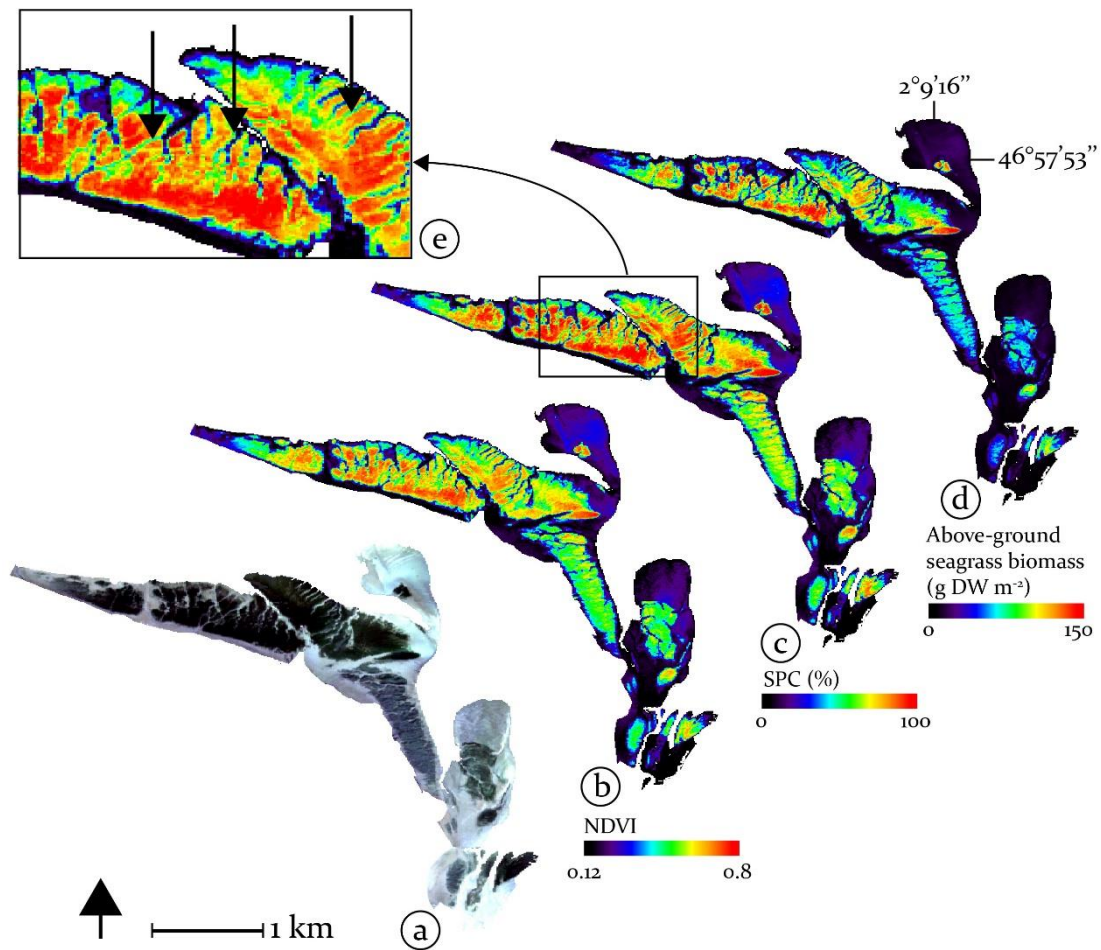


Figure 11 – The S2 image of the 14/09/2018 was used to map (a) the seagrass meadows in RGB color scale (R: 665 nm, G: 560 nm, B: 490 nm), (b) the NDVI, (c) the seagrass percent cover, and (d) the above-ground seagrass biomass. Pixels in white color were masked using NDVI thresholds ( $NDVI < 0.12$  or  $NDVI > 0.8$ , see text for more details). SPC, calculated from NDVI values as Equation 3 (d) Above-ground biomass ( $g DW m^{-2}$ ), calculated from NDVI values as Equation 4. (e) Zoom into a portion of the SPC map. Pixels in black color in all the figures correspond to No Data. Arrows indicate tidal channels within the meadow.

### 4.1.3 Epiphytes coverage

We performed an exploratory analysis to evaluate the ability of S2 to capture differences in epiphytes coverage through inspection of the slope between bands 740-783 nm. In contrast to the spectral bands used to map the NDVI, percent cover and biomass, these bands have a spatial resolution of 20 m. They are however the most pertinent spectral bands for the estimation of

epiphytes. We selected different pixels over areas with seagrass coverage higher than 95%. The samples were taken following an altitudinal transect, from the highest to the lowest parts along the seagrass meadow (Figure 12a). The spectral shape exhibited a degree of variability in the slope (740 - 783 nm) which is (at least partly) attributed to variations in epiphytes abundance (Figure 12b). The slope effectively increases seaward (Figure 12c), consistently with the hypothesis that the colonization of epiphytes is higher in the lowest part of the seagrass meadow, as a result of a longer time of emersion. The first results of this preliminary analysis suggest that the multispectral information available in S2 is able to provide a rough proxy of epiphytes abundance. Further tests on S2 images will be performed to also investigate the relationships between the height of the green peak and the abundance of epiphytes (Figure 6b).

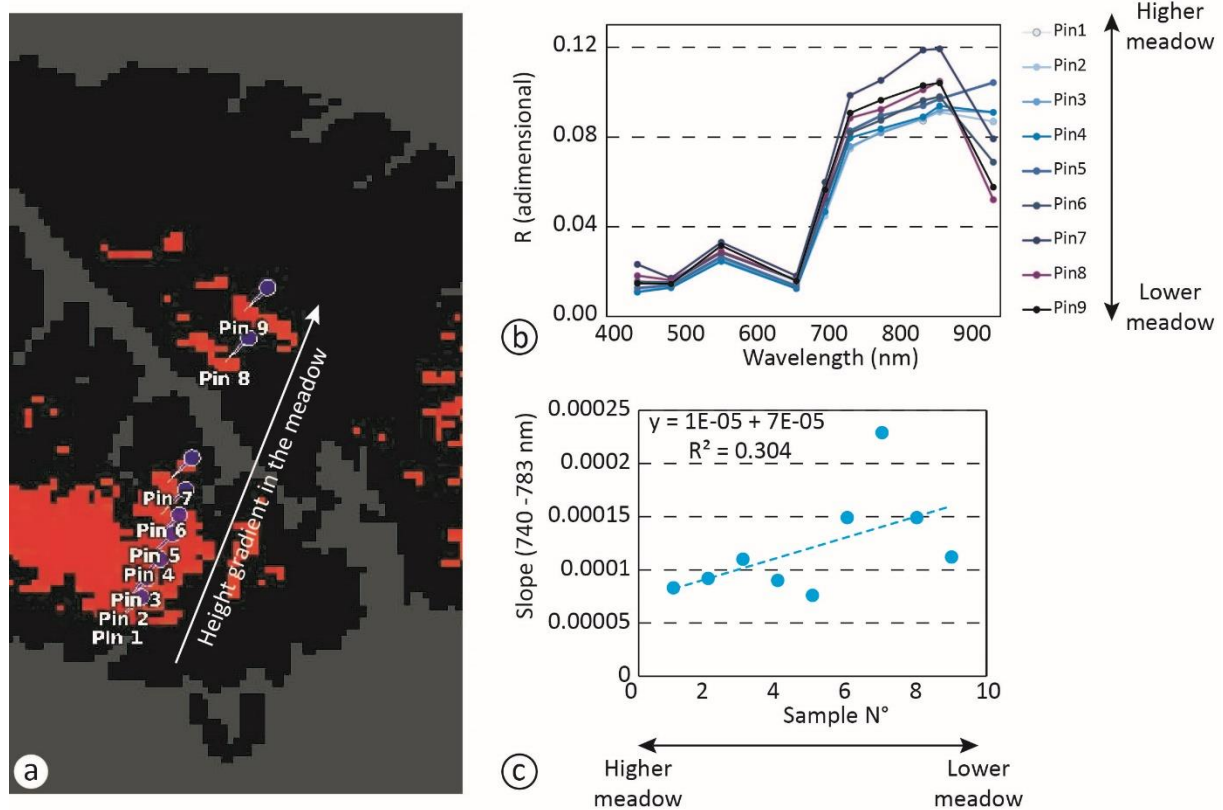


Figure 12 – (a) Position of the S2 samples selected to evaluate epiphytes coverage into the seagrass meadows. Pixels in red correspond to  $SPC \geq 95\%$ . The seaward transect was following a decreasing altitudinal direction: the first stations were located nearshore, at a higher altitude than the last stations. (b) R as a function of wavelength (nm) for the different samples considered in scheme a. (c) Slope estimated for the bands 740 to 783 nm for those samples.

## 4.2 Sub-tidal seagrass beds

### 4.2.1 Environmental conditions

Both sub-tidal areas showed similar seasonal patterns in all the parameters evaluated here (Figure 13). The Chl time-series displayed a major spring peak and coincides with the occurrence of phytoplankton blooms in subtropical and temperate latitudes, followed by a minor peak in autumn. The Chl concentration ranged from  $0.52 \pm 0.21 \text{ mg m}^{-3}$  (September) to  $1.64 \pm 0.73 \text{ mg m}^{-3}$  (March) in Glénan and from  $2.82 \pm 1.23 \text{ mg m}^{-3}$  (May) to  $1.23 \pm 0.36 \text{ mg m}^{-3}$  (September) off the Venice lagoon.  $K_d(490)$  followed the same pattern than Chl, ranging from  $0.15 \pm 0.05 \text{ m}^{-1}$  to  $0.072 \pm 0.015 \text{ m}^{-1}$  in Glénan, and from  $0.09 \pm 0.02 \text{ m}^{-1}$  and  $0.13 \pm 0.04 \text{ m}^{-1}$  off the Venice lagoon. The water column is then clearer during summer, which implies a higher contribution from the sea bottom in the signal recorded by the satellite.

The quality of passive satellite remote sensing is inherently dependent on cloud cover. The cloud fraction was therefore investigated to reject the periods during cloud cover is likely to impede top-of-atmosphere satellite observations. In Glénan, a lower fraction of clouds was observed in Spring-Summer (~60%) while the lowest cloud fraction period in Venice was shorter (July-August), with lower values (<50 %).

We also investigated the variability in aerosol optical thickness (AOT), which is inversely related to the atmospheric visibility (Vermote et al., 2002) and provides information about the atmospheric interferences which need to be removed prior to the water column correction. In both cases, a higher degree of atmospheric interference was observed during spring/summer/autumn, which means that it will be more challenging to perform a robust atmospheric correction of the satellite images acquired during those seasons.

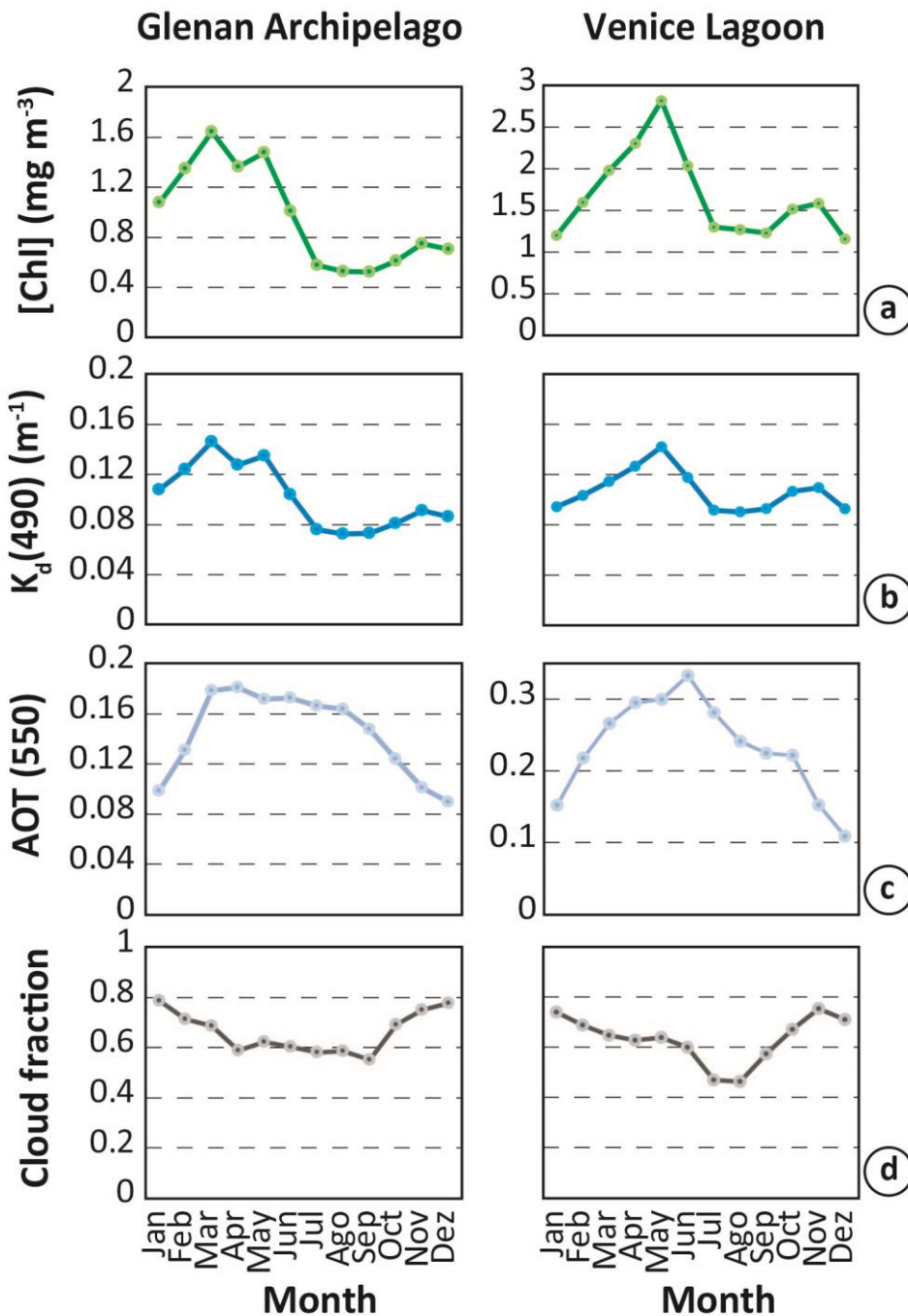


Figure 13 – Annual variability of environmental parameters obtained from satellite data in the Glénan Archipelago (left panels) and in Venice lagoon (right panels). (a) Chl concentration (in  $\text{mg m}^{-3}$ ); (b)  $K_d(490)$  (in  $\text{m}^{-1}$ ); (c) AOT (dimensionless) ; and (d) cloud fraction (dimensionless).

## 4.2.2 S2 maps of underwater seagrass, macroalgae and sand percent cover

One S2 image acquired in summer/2018 (on 31/07/2018) and corresponding to the Glénan Archipelago was used to produce sea bottom maps. This image was selected based on the following criteria: (i) low cloud cover, (ii) acquisition during the optimal season (see previous section), and (iii) synchronicity between low tide and satellite overflight in order to maximize the amplitude of bottom reflectance on the above-water data. The image passed through atmospheric correction routines using the C2RCC processor and was subsequently ran into the SWAM model. Figures 14-16 show the corresponding outputs maps of the percentage of cover of the 3 end-members considered here, namely sand, seagrass and macroalgae. From this preliminary series of runs, it can be observed that the seagrass meadow mainly occupies the central lagoon of the archipelago (Figure 14). A medium percent cover is generally observed, with some patches of high seagrass density around the biggest islands. In these areas (center lagoon and in the lee of the largest islands), the lower hydrodynamics favor the settlement of seagrass in soft substrates. Sand-dominated areas were predominant at the outer edges of the archipelago (Figure 15), where the higher hydrodynamics hinder the growth of benthic vegetation. Macroalgae mainly occurred in low/medium percentage of coverage, in the inner parts of the Archipelago where the seagrass extent was sub-optimal (Figure 16). The areas of high macroalgae percentage generally corresponded to narrow belts around the islands, in areas characterized by a rocky substrate.

Further runs of SWAM/Sen2Coral will be performed. The bounding ranges of the IOPs and of the water constituents will be set up according to the results of the *in situ* measurements performed in each region and season. A similar approach will be applied in the Venice Lagoon, though the water column correction in this site is expected to be more challenging than in the Glénan archipelago due to its overall higher turbidity and bio-optical complexity.

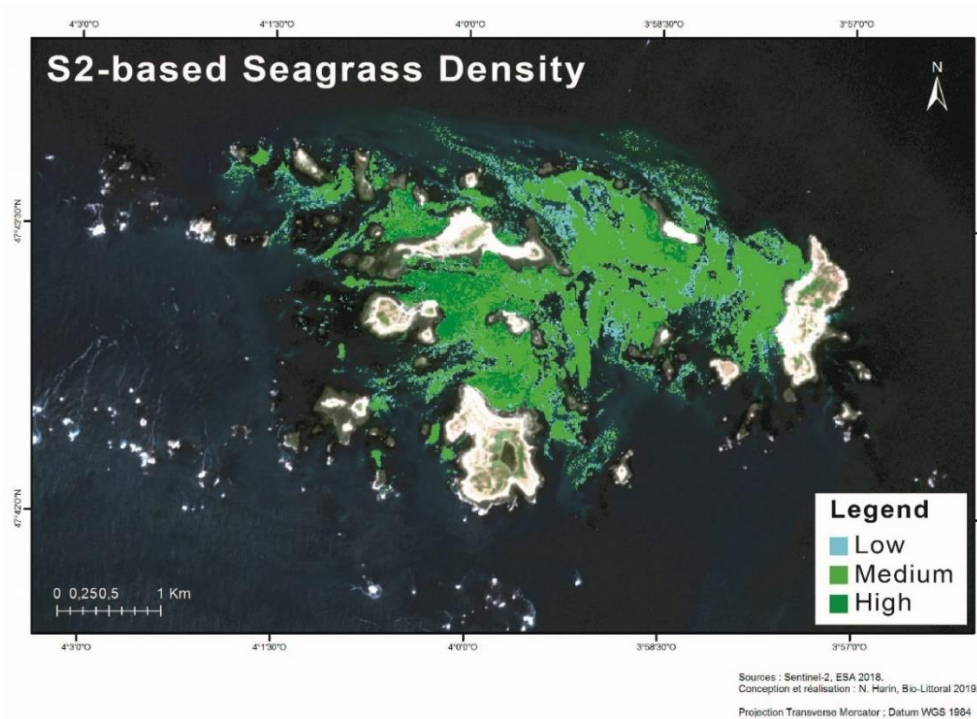


Figure 14 – S2-based Seagrass Density map in the Glénan archipelago produced from the 31/07/2018 image. The map is overlapping to the RGB S2 image.

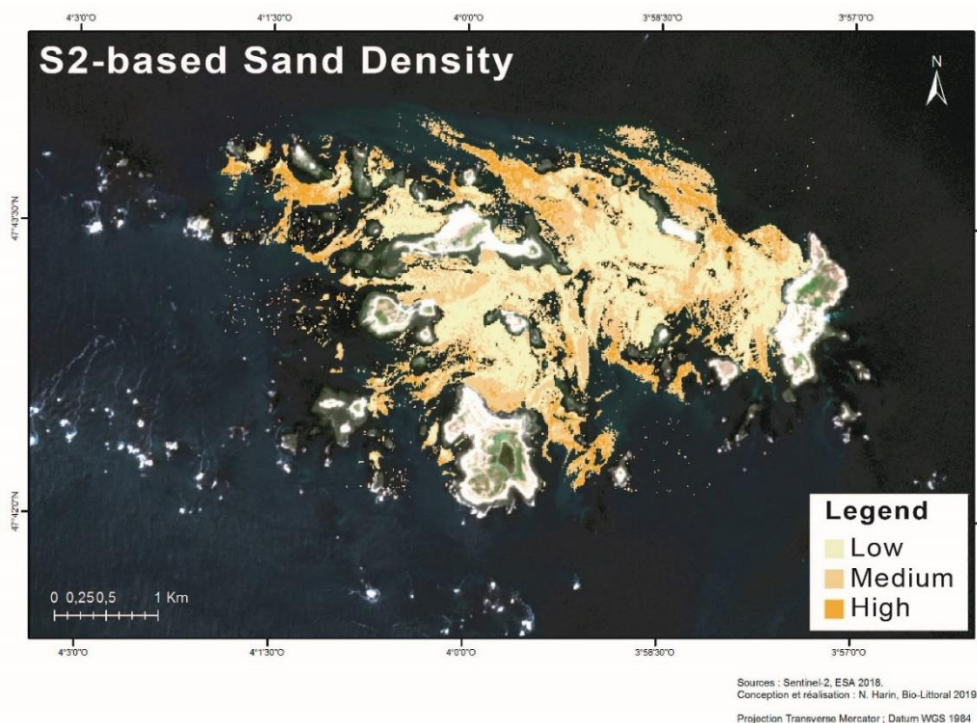


Figure 15 – S2-based Sand Density map in the Glénan archipelago produced from the 31/07/2018 image. The map is overlapping to the RGB S2 image

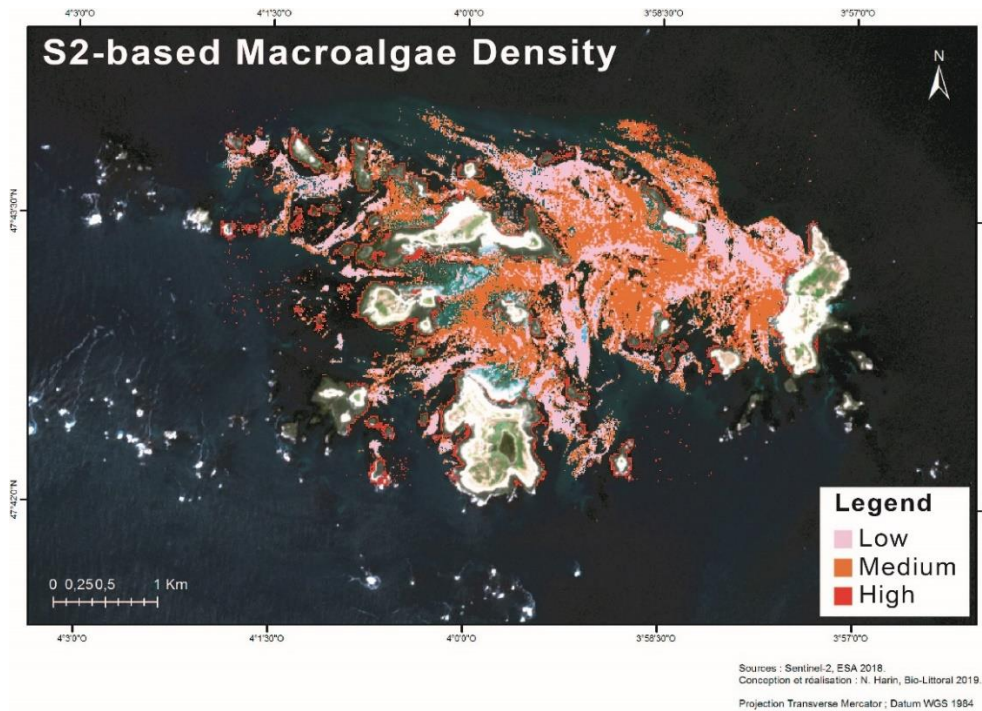


Figure 16 – S2-based Macroalgae Density map in the Glénan archipelago produced from the 31/07/2018 image. The map is overlapping to the RGB S2 image

## 5 Conclusions

- In the inter-tidal meadows, the NDVI was converted into seagrass percent cover (SPC) and seagrass biomass (SB) using a linear and a power model, respectively, whose parameters were obtained from concomitant *in situ* radiometric and biological measurements.
- At the period of maximum NDVI, the SPC ranged from 0 – 100%, with a mean SPC for the meadow of 44.7%. The area corresponding to SPC > 50% occupied a surface of 1.95 km<sup>2</sup>, from which about 0.74 km<sup>2</sup> had a cover > 80%. The seagrass above-ground biomass ranged from 2 – 166 g DW m<sup>-2</sup>, with a meadow-averaged biomass of 42 g DW m<sup>-2</sup>. Both SPC and SB maps displayed a patchy distribution.
- Due to the combination of two orbital cycles, where the S2 revisit time was 2-3 days, it allowed to characterize the annual variability of the seagrass meadow in 2018. The seagrass NDVI exhibited a seasonal cycle, characterized by growing season from mid-May to the beginning of December (12/05 – 3/12), a late-summer maximum (22/08 – 28/09), and a winter minimum.
- The variation of S2 reflectance spectral slope in the NIR along an altitudinal transect within the seagrass meadow was consistent with the distribution of epiphytes expected from *in situ* observations. This result, while very preliminary, suggests that S2 is able to detect the influence on epiphytes coverage. Given the spatial scale of the epiphytes (microns), the potential of S2 for epiphytes estimation in the inter-tidal seagrass meadow is very encouraging. Additional investigations will be performed to evaluate the suitability of epiphytes' estimation using the spectral information provided by the green reflectance peak around 560 nm.
- For the sub-tidal sites, the analysis of long-term satellite time-series highlighted similar seasonal variability in the Glénan Archipelago and off the Venice lagoon. This analysis pointed summer (Jul-Sep) as the best season of the year to map sub-tidal meadows using satellite remote sensing. During this period, the water is clearer and the cloud cover is lower. However, higher atmospheric interference is expected in this season.
- Sen2Coral/SNAP is able to retrieve sea bottom information from S2 images using specific end-members adjusted to the study areas.
- In the Glénan archipelago, seagrasses were mostly found in the center lagoon and in the lee of the largest islands. Sand-dominated areas were predominant in the outer edges of the archipelago. Macroalgae was mainly represented by low/medium percentage of coverage in the inner part of the archipelago, and by high coverage in restricted rocky areas around the islands.
- Additional runs of SWAM/Sen2Coral will be performed with adjusted boundaries of IOPs and water constituents according to the *in situ* measurements. A similar approach will be performed in the Venice Lagoon.

## 6 Publications

We submitted a scientific manuscript to the journal „Remote Sensing of Environment” on the 09/04/2019. The manuscript is currently under revision under the Number RSE-D-19-00625. The manuscript’s title and authors list is provided below.

Manuscript title: **Sentinel-2 remote sensing of intertidal seagrass**

Authors: **Maria Laura Zoffoli<sup>1</sup>, Pierre Gernez<sup>1</sup>, Philippe Rosa<sup>1</sup>, Anthony Le Bris<sup>1,2</sup>, Vittorio Brando<sup>3</sup>, Anne-Laure Barillé<sup>4</sup>, Nicolas Harin<sup>4</sup>, Steef Peters<sup>5</sup>, Kathrin Poser<sup>5</sup>, Lazaros Spaias<sup>5</sup> and Laurent Barillé<sup>1</sup>**

<sup>1</sup>Université de Nantes, Laboratoire Mer Molécules Santé, Faculté des Sciences, 2 rue de la Houssinière, 44322, Nantes, France

<sup>2</sup>Currently at Ecology and Environment department (EENVI), Algae Technology and Innovation Centre (CEVA), 22610, Pleubian, France

<sup>3</sup>Institute of Atmospheric Sciences and Climate, National Research Council of Italy (CNR-ISAC), 00133, Rome, Italy

<sup>4</sup>Bio-littoral, Faculté des Sciences et des Techniques, B.P. 92 208, 44322, Nantes, France

<sup>5</sup>Water Insight, 6709 PG 22, Wageningen, The Netherlands

## 7 References

- Bargain, A., 2012. Etude de la structure et de la dynamique des herbiers de *Zostera noltii* par télédétection multi et hyperspectrale. Université de Nantes.
- Bargain, A., Robin, M., Le Men, E., Huete, A., Barillé, L., 2012. Spectral response of the seagrass *Zostera noltii* with different sediment backgrounds. *Aquat. Bot.* 98, 45–56. <https://doi.org/10.1016/j.aquabot.2011.12.009>
- Barillé, L., Robin, M., Harin, N., Bargain, A., Launeau, P., 2010. Increase in seagrass distribution at Bourgneuf Bay (France) detected by spatial remote sensing. *Aquat. Bot.* 92, 185–194. <https://doi.org/10.1016/j.aquabot.2009.11.006>
- Brando, V.E., Anstee, J.M., Wettle, M., Dekker, A.G., Phinn, S.R., Roelfsema, C., 2009. A physics based retrieval and quality assessment of bathymetry from suboptimal hyperspectral data. *Remote Sens Environ.* 113, 755–770. doi:10.1016/j.rse.2008.12.003
- Bricker, S., Ferreira, J., Simas, T., 2003. An integrated methodology for assessment of estuarine trophic status. *Ecological Modelling* 169, 39–60.
- Caballero, I., Stumpf, R.P., Meredith, A., 2019. Preliminary Assessment of Turbidity and Chlorophyll Impact on Bathymetry Derived from Sentinel-2A and Sentinel-3A Satellites in South Florida. *Remote Sensing*, 11, 645. <https://doi.org/10.3390/rs11060645>.
- Casal, G., Monteys, X., Hedley, J., Harris, P., Cahalane, C., McCarthy, T., 2019. Assessment of empirical algorithms for bathymetry extraction using Sentinel-2 data. *J. Remote Sens.* 40, 2855–2879. <https://doi.org/10.1080/01431161.2018.1533660>.
- Dekker, A., Brando, V., Anstee, J., Fyfe, S., Malthus, T., Karpouli, 2006. Remote sensing of seagrass ecosystem: use of spaceborne and airborne sensors. In: A. Larkum, R. Orth, C. Duarte (Eds.), *Seagrasses: biology, ecology, and conservation*, pp. 347–359. The Netherlands: Springer. 691p.
- Diaz-Pulido, G., Gouezo, M., Tilbrook, B., Dove, S., Anthony, K.R.N., 2011. High CO<sub>2</sub> enhances the competitive strength of seaweeds over corals. *Ecol. Lett.* <https://doi.org/10.1111/j.1461-0248.2010.01565.x>
- Dutertre, M., 2012. Structuration des habitats benthiques des substrats meubles subtidiaux de la frange côtière de Bretagne sud en relation avec les facteurs environnementaux. RST/IFREMER/ODE/DYNECO/EB/12-03/MD. <https://archimer.ifremer.fr/doc/00092/20352/>
- Dutertre, M., Beninger, P.G., Barillé, L., Papin, M., Rosa, P., Barillé, A.-L., Haure, J., 2009. Temperature and seston quantity and quality effects on field reproduction of farmed oysters, *Crassostrea gigas*, in Bourgneuf Bay, France. *Aquat. Living Resour.* 22, 319–329. <https://doi.org/10.1051/alr/2009042>
- Echappé, C., Gernez, P., Méléder, V., Jesus, B., Cognie, B., Decottignies, P., Sabbe, K., Barillé, L., 2018. Satellite remote sensing reveals a positive impact of living oyster reefs on microalgal biofilm development. *Biogeosciences* 15, 905–918. <https://doi.org/10.5194/bg-15-905-2018>
- ESA, 2015. SENTINEL-2 User Handbook. <https://doi.org/10.13128/REA-22658>

- Foden, J., Brazier, D.P., 2007. Angiosperms (seagrass) within the EU water framework directive: A UK perspective. *Marine pollution bulletin*. 55, 181–95. [10.1016/j.marpolbul.2006.08.021](https://doi.org/10.1016/j.marpolbul.2006.08.021)
- Frankovich, T.A., Fourqurean, J.W., 1997. Seagrass epiphyte loads along a nutrient availability gradient, Florida Bay, USA. *Marine Ecology Progress Series* 159, 37–50.
- Gernez, P., Barillé, L., Lerouxel, A., Mazeran, C., Lucas, A., Doxaran, D., 2014. Remote sensing of suspended particulate matter in turbid oyster-farming ecosystems. *J. Geophys. Res. Ocean.* 119, 7277–7294. <https://doi.org/10.1002/2014JC010055>
- Huete, A.R., 1988. A Soil-Adjusted Vegetation Index (SAVI). *Remote Sens. Environ.* 25, 295–309.
- Jesus, B., Rosa, P., Mouget, J.L., Méléder, V., Launeau, P., Barillé, L., 2014. Spectral-radiometric analysis of taxonomically mixed microphytobenthic biofilms. *Remote Sens Environ.* 140, 196–205. [doi:10.1016/j.rse.2013.08.040](https://doi.org/10.1016/j.rse.2013.08.040)
- Jönsson, P., Eklundh, L., 2004. TIMESAT - A program for analyzing time-series of satellite sensor data. *Comput. Geosci.* 30, 833–845. <https://doi.org/10.1016/j.cageo.2004.05.006>
- Kaufman, Y.J., Tanré, D., 1992. Atmospherically resistant vegetation index (ARVI) for EOS-MODIS. *IEEE Trans. Geosci. Remote Sens.* 30, 261–270.
- Lee, Z., Carder, K. L., Mobley, C. D., Steward, R. G., & Patch, J. F., 1999. Hyperspectral remote sensing for shallow waters: 2. Deriving bottom depths and water properties by optimization. *Applied Optics*, 38, 3831–3843.
- Milton, E.J., Schaeppman, M.E., Anderson, K., Kneubühler, M., Fox, N.P., 2007. Progress in field spectroscopy. *Int. Geosci. Remote Sens. Symp.* 113, S92–S109. <https://doi.org/10.1109/IGARSS.2006.509>
- Murray, L., Sturgis, R.B., Bartleson, R.D., Severn, W., Kemp, W.M., 2000. Scaling submersed plant community responses to experimental nutrient enrichment In: Bortone SA (Ed.), *Seagrasses: Monitoring, ecology, physiology, and management*. CRC Press, Boca Raton, FL pp. 241–257.
- Neckles, H.A., Wetzel, R.L., Orth, R.J., 1993. Relative effects of nutrient enrichment and grazing on epiphyte-macrophyte (*Zostera marina* L.) dynamics. *Oecologia* 93, 285–295.
- Nelson, W.G., 2017. Development of an epiphyte indicator of nutrient enrichment: threshold values for seagrass epiphyte load. *Ecol Indic.* 74, 343–356. [doi:10.1016/j.ecolind.2016.11.035](https://doi.org/10.1016/j.ecolind.2016.11.035).
- Neto, J.M., Barroso, D., Barría, P., 2013. Seagrass Quality Index (SQI), a Water Framework Directive compliant tool for the assessment of transitional and coastal intertidal areas. *Ecological Indicators*, 30, 130–137. [10.1016/j.ecolind.2013.02.015](https://doi.org/10.1016/j.ecolind.2013.02.015).
- Perkins, R.G., Williamson, C.J., Brodie, J., Barillé, L., Launeau, P., Lavaud, J., 2016. Microspatial variability in community structure and photophysiology of calcified macroalgal microbiomes revealed by coupling of hyperspectral and high-resolution fluorescence imaging. *Scientific Reports*. 6, 22343. [doi:10.1038/srep22343](https://doi.org/10.1038/srep22343)
- Phillips, G., Eminson, D., Moss, B., 1978. A mechanism to account for macrophyte decline in progressively eutrophicated freshwaters. *Aquatic Botany* 4, 103–126.

- Scapin, L., Cavraro, F., Malavasi, S., Riccato, F., Zucchetta, M., Franzoi, P., 2018. Linking pipefishes and seahorses to seagrass meadows in the Venice lagoon: Implications for conservation. *Aquatic Conserv: Mar Freshw Ecosyst*, 28:282–295. DOI: 10.1002/aqc.2860
- Sims, D., Gamon, A., 2002. Relationships between leaf pigment content and spectral reflectance across a wide range of species, leaf structures and developmental stages. *Remote Sens. Environ.* 81, 337–354.
- Tucker, C.J., 1979. Red and photographic infrared linear combinations for monitoring vegetation. *Remote Sens. Environ.* 8, 127–150. [https://doi.org/10.1016/0034-4257\(79\)90013-0](https://doi.org/10.1016/0034-4257(79)90013-0)
- Valle, M., Chust, G., del Campo, A., Wisz, M.S., Olsen, S.M., Garmendia, J.M., Borja, Á., 2014. Projecting future distribution of the seagrass *Zostera noltii* under global warming and sea level rise. *Biol. Conserv.* 170, 74–85. <https://doi.org/10.1016/j.biocon.2013.12.017>
- Valle, M., Palà, V., Lafon, V., Dehouck, A., Garmendia, J.M., Borja, Á., Chust, G., 2015. Mapping estuarine habitats using airborne hyperspectral imagery, with special focus on seagrass meadows. *Estuar. Coast. Shelf Sci.* 164, 433–442. <https://doi.org/10.1016/j.ecss.2015.07.034>
- Vermaat, J.E., Verhagen, F.C.A., 1996. Seasonal variation in the intertidal seagrass *Zostera noltii* Hornem.: Copuling demographic and physiological patterns. *Aquat. Bot.* 52, 259–281. [https://doi.org/10.1016/0304-3770\(95\)00510-2](https://doi.org/10.1016/0304-3770(95)00510-2)
- Vermote, E.F., Vibert, S., Kilcoyne, H., Hoyt, D., Zhao, T., 2002. Suspended matter - visible/infrared imager/radiometer suite algorithm theoretical basis document. Maryland: Raytheon Systems Company, Information Technology and Scientific Services. SBRS Document # Y2390.
- Warren, M.A., Simis, S.G.H., Martinez-Vicente, V., Poser, K., Bresciani, M., Alikas, K., Spyarakos, E., Giardino, C., Ansper, A., 2019. Assessment of atmospheric correction algorithms for the Sentinel-2A MultiSpectral Imager over coastal and inland waters. *Remote Sens. Environ.* 225, 267–289. <https://doi.org/10.1016/j.rse.2019.03.018>
- Wei, J., Lee, Z., Garcia, R., Zoffoli, L., Armstrong, R.A., Shang, Z., Sheldon, P., Chen, R.F., 2018. An assessment of Landsat-8 atmospheric correction schemes and remote sensing reflectance products in coral reefs and coastal turbid waters. *Remote Sens. Environ.* 215, 18–32. <https://doi.org/10.1016/j.rse.2018.05.033>
- Wettle, M., Brando, V. E., 2006. SAMBUCA—Semi-analytical model for bathymetry, unmixing and concentration assessment. CSIRO Land and Water Science Report 22/06 Canberra: CSIRO Land and Water.
- Wood, N., Lavery, P., 2000. Monitoring seagrass ecosystem health—the role of perception in defining health and indicators. *Ecosystem Health* 6, 134–148.
- Zoffoli, M.L., Frouin, R., Kampel, M., 2014. Water Column Correction for Coral Reef Studies by Remote Sensing. *Sensors*, 16881–16931; doi:10.3390/s140916881